Elsevier Editorial System(tm) for Combustion and Flame
Manuscript Draft

Manuscript Number:

Title: Large Eddy Simulation/Probability Density Function Simulations of Bluff Body Stabilized Flames

Article Type: Full Length Article

Keywords: turbulent nonpremixed flame, bluff-body flow, LES/PDF simulation, finite volume/Lagrangian particle algorithms for turbulent reactive flow simulation, local extinction

Corresponding Author: Dr. Pavel P Popov, Ph.D.

Corresponding Author's Institution: University of California-Irvine

First Author: Pavel P Popov, Ph.D.

Order of Authors: Pavel P Popov, Ph.D.; Stephen B Pope, Ph.D.

Abstract: This work presents large eddy simulation/probability density function (LES/PDF) simulation results for the Sandia/Sydney series of bluff-body stabilized CH_4/H_2 flames. Results are presented for the flames HM1, HM2 and HM3, using the 19-species ARM2 reduced chemical mechanism, and comparison is made with previous numerical simulations of the same flames. When compared to previous numerical studies of these bluff-body flames, the present simulation shows considerable improvement, particularly in the downstream regions of the flow. The simulations are shown to be sensitive to the treatment of heat transfer to the bluff-body face, with better agreement in the temperature profiles achieved with the addition of a Dirichlet temperature boundary condition.

Suggested Reviewers: Venkatramanan Raman Ph.D.
Associate Professor, Aerospace Engineering and Engineering Mechanics, UT-Austin
v.raman@mail.utexas.edu
Has performed simulations on the Sydney bluff-body flame

Peyman Givi Ph.D.
Professor, Chemical and Petroleum Engineering, University of Pittsburgh
pgivi@pitt.edu
Has made significant contributions to the field of numerical methods for turbulent reactive flow simulations.

Bart Merci Ph.D.
Lecturer, Department of Flow, Heat and Combustion Mechanics, Ghent University
Bart.Merci@UGhent.be
Has performed numerical simulations on the Sandia-Sydney bluff-body flames

Assaad R Masri Ph.D.
Professor, Aerospace, Mechanical and Mechatronic Engineering, University of Sydney
assaad.masri@sydney.edu.au
Has performed the experiments which are simulated numerically in this paper.

Large Eddy Simulation/Probability Density Function Simulations of Bluff Body Stabilized Flames

Pavel P. Popov
Stephen B. Pope
Sibley School of Mechanical and Aerospace Engineering
Cornell University
Ithaca, NY 14853, USA

Dec 10, 2012

Abstract

This work presents large eddy simulation/probability density function (LES/PDF) simulation results for the Sandia/Sydney series of bluff-body stabilized CH_4/H_2 flames. Results are presented for the flames HM1, HM2 and HM3, using the 19-species ARM2 reduced chemical mechanism, and comparison is made with previous numerical simulations of the same flames. When compared to previous numerical studies of these bluff-body flames, the present simulation shows considerable improvement, particularly in the downstream regions of the flow. The simulations are shown to be sensitive to the treatment of heat transfer to the bluff-body face, with better agreement in the temperature profiles achieved with the addition of a Dirichlet temperature boundary condition.

1 Introduction

In the study of computational methods for turbulent reactive flows, the probability density function (PDF) chemistry modeling approach [1] is highly effective, due to the fact that there is no need for modeling of highly non-linear chemical source term [2]. In a large eddy simulation/probability density function (LES/PDF) algorithm [3], this advantage of the PDF chemistry model is coupled to the advantages of LES codes, which need no modeling for the large hydrodynamic scales which do not exhibit universal behavior [4]. As a result, modern LES/PDF codes are highly successful at simulating laboratory scale turbulent reactive flows [5,6,8, 9, 22].

In the present study, we apply a state of the art LES/PDF algorithm to the Sandia/Sydney series of CH_4/H_2 bluff body stabilized flames [11], in particular the flames HM1, HM2 and HM3. These flames feature a hydrodynamically

complex flow with a recirculation region attached to the bluff body face - a stabilization mechanism used in many technical applications - and local extinction for the cases HM2 and HM3. These features make the Sandia/Sydney bluff body flames both physically relevant and a natural application for an LES-based simulation, as opposed to a Reynolds-averaged Navier-Stokes-based solution.

The Sandia-Sydney bluff body series of flames, especially HM1, have previously been simulated by a variety of computational methods. Reynolds-averaged Navier-Stokes/Probability Density Function (RANS/PDF) solutions, using detailed chemistry (all the species in the chemical mechanism are tracked independently, subject to conservation of chemical elements), have been performed by Liu et al. [12] and Merci et al. [13]. A variety of large eddy simulation solutions exist, with chemistry modeling provided either via a steady-state flamelet model in the LES code, used by Kempf et al. [14], the direct quadrature method of moments used by Raman et al. [9], or via a particle probability density function (PDF) method, similar to the one used in the present study, either with detailed chemistry such as in the study of James et al. [15], or with a two-dimensional PDF sample space, consisting of mixture fraction and a reaction progress variable, in the work of Raman et al. [16,9].

Of the abovementioned works, [12] and [13] are the only ones which have performed simulations for the higher velocity flames HM2 and HM3 - the rest yield results for HM1 only. Previous researchers have found that the agreement with experimental data is best for the flame HM1, and deteriorates progressively for the faster flames HM2 and HM3, and also that the agreement is worse for locations which are far downstream in the axial direction.

In the present work, we perform LES/PDF simulations of the bluff body flames with reduced chemistry, using the ARM2 chemical mechanism, and compare our results with those of Liu et al. [12] and Merci et al. [13], as well as with the LES/PDF results of Raman et al. [16], which for the HM1 case yield best agreement with experiment among the studies listed above. As we shall see, the new computaional results show considerable improvement over these previous studies, especially in the downstream regions of the domain.

The rest of this paper is organized as follows: in section 2 we describe the equations governing the LES/PDF procedure used in the present study. Simulation details are provided in section 3, and the simulation results are presented and discussed in section 4. Finally, in section 5 we draw conclusions from the present set of simulation and their comparison to previous numerical results.

2 Equations Solved by the LES/HPDF Code

The LES/HPDF code used to simulate the bluff-body flame consists of two components: a finite volume (FV) LES code, based on a standalone-LES algorithm described by Pierce and Moin [17,16], and a Lagrangian particle PDF code, described by Wang and Pope [22]. The LES component of the LES/HPDF code solves the continuity and momentum equations

$$\frac{\partial \overline{\rho}}{\partial t} + \frac{\partial \overline{\rho} \tilde{u}_j}{\partial x_j} = 0 \tag{1}$$

$$\frac{\partial \left(\overline{\rho} \tilde{u}_j\right)}{\partial t} + \frac{\partial (\overline{\rho} \tilde{u}_i \tilde{u}_j)}{\partial x_i} = -\frac{\partial \overline{p}}{\partial x_j} + 2\frac{\partial}{\partial x_i}\left(\overline{\rho}\left(\widetilde{\nu} + \widetilde{\nu}_T\right)\left(\tilde{S}_{ij} - \frac{1}{3}\tilde{S}_{kk}\delta_{ij}\right)\right), \tag{2}$$

where $\overline{p}$ and $\overline{\rho}$ are the LES resolved pressure and density, $\tilde{u}_j$, $\widetilde{\nu}$ and $\tilde{D}$ the Favre-averaged resolved velocity, molecular viscosity and molecular diffusivity, $\tilde{S}_{ij}$ is the resolved strain rate, and $\widetilde{\nu}_T$ and $\tilde{D}_T$ are the turbulent viscosity and diffusivity, respectively. The molecular viscosity and diffusivity are evaluated by the power law

$$\widetilde{\nu} = \nu_0 \left(\frac{\widetilde{T}}{300K}\right)^{1.69}, \ \frac{\widetilde{\nu}}{\widetilde{D}} = \sigma, \ \sigma = 0.82, \nu_0 = 1.42 \times 10^{-5} \left[\frac{m^2}{s}\right], \tag{3}$$

where the exponent in the power law is based on a curve fit to a CHEMKIN laminar flame calculation [22], and ν_0, σ are based on the properties of a stoichiometric fuel/air mixture at $300K$.

The turbulent viscosity and diffusivity are evaluated by the Dynamic Smagorinsky procedure, with Δ denoting the filter size (equal to the grid cell size) [19,17,18]. The LES component of the code also evaluates the scalar mixing frequency, Ω, defined as

$$\Omega = C_\phi \frac{\tilde{D}_T + 2\tilde{D}}{\Delta^2}, \tag{4}$$

which is used to model mixing in the PDF code, by the IEM procedure, with the mixing constant $C_\phi = 2.0$.

The PDF code advances the chemical compositions. In particular, we use ϕ_α to denote the composition vector, which in the present work consists of the specific moles of the 19 species in the ARM2 chemical mechanism, with the addition of enthalpy. Then, using ψ_α to denote points in the sample space of the composition vector ϕ_α, and using $f\left(\psi; \mathbf{x}, t\right)$ to denote the mass-weighted PDF of chemical compositions, conditional on the resolved velocity field [10,20], the modeled evolution equation for $f\left(\psi; \mathbf{x}, t\right)$ has the form

$$\frac{\partial f}{\partial t} + \frac{\partial}{\partial x_i}\left(f\tilde{u}_i\right) = \frac{\partial}{\partial x_i}\left(\tilde{D}_T \frac{\partial f}{\partial x_i}\right) + \frac{\partial}{\partial \psi_\alpha}\left(f\Omega\left(\psi_\alpha - \tilde{\phi}_\alpha\right)\right)$$

$$-\frac{\partial}{\partial \psi_\alpha}\left(f\frac{1}{\bar{\rho}}\frac{\partial}{\partial x_i}\left(\bar{\rho}\tilde{D}\frac{\partial \tilde{\phi}_\alpha}{\partial x_i}\right)\right) + \frac{\partial}{\partial \psi_\alpha}\left(f S_\alpha\left(\psi\right)\right), \tag{5}$$

where the terms on the right hand side of eq.(5) are, in order, turbulent diffusion using the turbulent diffusivity hypothesis, turbulent mixing using the IEM mixing model [24], molecular diffusion, the reaction source term.

The evolution of eq.(5) is calculated via a Monte Carlo approximation [1], in order to avoid discretization in a high-dimensional space. The properties of an ensemble of Lagrangian particles are initialized throughout the computational domain and evolve by the following set of stochastic differential equations (SDEs):

$$dX_j^* = \left[\widetilde{u}_j + \frac{1}{\overline{\rho}} \frac{\partial \left(\overline{\rho} \widetilde{D}_T \right)}{\partial x_j} \right]^* dt + \left[2 \tilde{D}_T^* \right]^{1/2} dW_j^*, \tag{6}$$

$$d\phi_\alpha^* = -\Omega^* \left(\phi_\alpha^* - \widetilde{\phi}_\alpha^* \right) dt + \left[\frac{1}{\overline{\rho}} \frac{\partial}{\partial x_j} \left(\overline{\rho} \widetilde{D} \frac{\partial \widetilde{\phi}_\alpha}{\partial x_j} \right) \right]^* dt + S_\alpha \left(\boldsymbol{\phi}^* \right) dt. \tag{7}$$

where the term dW_j^* in eq.(6) denotes a Wiener increment, and the three terms on the right hand side of eq.(7) denote respectively turbulent mixing (in this case represented by the IEM model), molecular diffusion, and chemical reaction [21]. The superscript * in eqs.(6,7) is used to denote particle-based quantities. In the absence of numerical errors, the evolution of the mass-weighted PDF of the particle ensemble is identical to eq.(5), which is the PDF chemistry model which we aim to approximate numerically.

More details on the LES and PDF algorithms, and on their coupling, can be found in [17,22,23].

3 Simulation Details

The Sandia-Sydney Bluff-Body flames HM1, HM2 and HM3 consist of a fuel jet of diameter $3.6mm$ inside a bluff body of diameter $50mm$, itself located inside a square wind tunnel with sides of $150mm$. The fuel is $CH_4 : H_2$ in $1 : 1$ molar ratio, the coflow is air, and both fuel and coflow are at a temperature of $300K$. In all cases, the coflow bulk velocity is $40m/s$, and the fuel jet bulk velocity is $118m/s$ for the flame HM1, $178m/s$ for the flame HM2, and $212m/s$ for HM3; these fuel jet velocities correspond to 50%, 75% respectively 90% of the blowoff velocity [11].

The computational domain for the present simulation is $x \in [0, 20R_B]$, $r \in [0, 3.39R_B]$, where R_B is the bluff-body radius, and $r = 3.39R_B$ corresponds to a hydraulic diameter equal to that of the square wind tunnel. The grid size is $192 \times 128 \times 96$ in x, r, θ cylindrical coordinates - of the 128 cells in the radial direction, 85 discretize the bluff-body, 15 discretize the jet, and 28 discretize the coflow (the grid cell spacing in the radial direction increases considerably past $r = R_B$). Simulations are run for 30000 time steps of length $6 \times 10^{-6}s$ each, which corresponds to 14.5 flow-through times based on the coflow velocity; the number of particles per cell is set to 40.

The $19-$species reduced chemical mechanism ARM2 [7] is used to model chemistry; this mechanism has previously been used successfully by Liu et al.

[12] for RANS/PDF simulations of the same series of flames. In Situ Adaptive Tabulation (ISAT) [25] is used for speedup of the chemical reaction calculations.

The velocity inlet boundary conditions for the fuel jet and the coflow are determined from an incompressible pipe flow simulation, with the pipe having either a circular or an annular cross section, for the jet and coflow, respectively. No-slip boundary conditions are enforced on the bluff-body surface and on the radial boundary of the cylindrical domain ($r = 3.39R_B$). We shall test two separate temperature boundary conditions for the bluff-body face. The first assumes that the bluff-body face is adiabatic, analogously to the simulations of Liu et al. [12], Merci et al. [13], and Raman et al. [16]; an optional Dirichlet temperature boundary condition has also been implemented by setting the temperature of all particles up to half a grid cell downstream axially from the bluff body to the mean bluff-body temperature measured from experimental data (respectively $953K$, $1007K$ and $1050K$ for the HM1, HM2 and HM3 flames). As we shall see in the next section, the inclusion of this boundary condition gives an improvement in the accuracy of temperature profiles close to the bluff-body over simulations without it, in which the bluff-body surface is adiabatic.

We note that the present simulation does not resolve the near-wall region, or use wall functions for heat transfer to the bluff-body face, and hence the Dirichlet temperature boundary condition described above is equivalent to taking the thermal resistance of the unresolved near wall-region to be zero. On the other hand, the standard adiabatic temperature boundary condition used in previous studies is equivalent to infinite thermal resistance in the near wall-region. These two boundary conditions, therefore, bound the actual thermal resistance of the near-wall region from above and below; as we shall see, in the present simulation the temperature profile yields better agreement with experiment when the Dirichlet boundary condition is used.

4 Results and Discussion

In this section, we present results for the bluff-body flames. Statistics are calculated over the second half of the simulation time interval, at which point the flow is statistically stationary; statistical averaging is performed in time and in the θ direction. Comparison is made with experimental data and, wherever the data are available, with previous computational results by Raman et al. [16], Liu et al. [12], and Merci et al. [13]. The simulation from Merci et al. which is used for comparison here is the one with the EMST mixing model and $C_\phi = 1.5$, whose Favre-averaged profiles give the best agreement with experimental data. For the flame HM1, we make a comparison between the temperatures obtained using the imposed temperature boundary condition discussed in the previous section, and those obtained without it (which imply that the bluff-body face is adiabatic). Unless otherwise specified, the results presented are from a simulation with the imposed temperature at the bluff-body face.

4.1 Results for Flame HM1

Figure 1 shows radial plots of Favre-averaged axial and radial velocity at three different axial locations, $x/D_B = 0.2, x/D_B = 0.6$ and $x/D_B = 1.4$. Here, the results are scaled by a factor of 108/118, in order to provide a valid comparison with the experimental velocity data provided by previous numerical studies, which are reported for the slightly slower flame HM1e, whose jet velocity is $108m/s$ instead of $118m/s$ for flame HM1. As we can see, all simulations give a good prediction of the mean axial velocity, with the exception of that of Merci et al., which considerably overpredicts the axial velocity close to the centerline for $x/D_B = 0.6$. The radial velocity plots show greater sensitivity to the simulation, and the agreement between simulations and experiment is worse here, especially at $x/D_B = 1.4$, where the two RANS/PDF calculations (Liu et al. and Merci et al.) underpredict the mean radial velocities by as much as $4m/s$ around $r = 10mm$. The LES calculations - that of the present study and that of Raman et al. - yield a better prediction of the mean radial velocity at that location, which is to be expected due to the advantages of LES over RANS in simulating more hydrodynamically complex flows, such as the present bluff-body flame. It should also be noted that the mean velocity profiles yielded by the two LES calculations are in close agreement with each other, which can be explained by the fact that both are based on the same incompressible LES solver and turbulence modeling described in Pierce and Moin [17], and that the grid resolution is similar in the two studies (Raman et al. use a $256 \times 128 \times 32$ grid).

Figure 2 shows radial plots of the root-mean-squares (RMS) of the axial and radial velocity fluctuations at the same axial locations: here, the RMS values are calculated based on the resolved velocity only. Again, the results are scaled by a factor of 108/118. Here the main difference between simulations and experiment is in the prediction of peak values of the rms velocity close to the centerline - at $x/D_B = 0.2$, the present simulation is in good agreement with the experimental rms axial velocity, and does not overpredicts the peak rms radial velocity as much as the simulation of Raman et al. At $x/D_B = 1.4$, all simulations underpredict the rms axial velocity for $r < 5mm$ and the rms radial velocity for $r < 10mm$.

Figures 3 and 4 show radial profiles of the Favre-averaged mixture fractions, and the RMS of its fluctuations respectively. Unlike the velocity RMS values, the mixture fraction RMS includes the contributions of both the resolved and residual mixture fraction fields. The present calculation is in generally in good agreement with experimental data at all axial locations - the same can be said of Raman et al.'s results. Merci et al.'s results are also in good agreement with experiment, except close to the centerline at $x/D_B = 0.6, 1.3$ where the peak mean mixture fraction is overpredicted. Finally, Liu et al. considerably underpredict the experimental data at the downstream locations $x/D_B = 1.8, 2.4$. We should also note that the present simulation overpredicts the mean mixture fraction at the upstream locations $x/D_B = 0.26, 0.6$, for $r > R_B$, where its mean mixture fraction drops off to zero more slowly than the experimental data and

the other calculations. This is most likely due to insufficient resolution in the outer shear layer, and as we shall see shortly, has an effect on the scalar profiles. While these discrepancies appear to be small, it should be appreciated that they appear around the stoichiometric mixture fraction, $\xi_{st} \approx 0.052$. Consequently, the impact on species may be more substantial, as is evident from the profiles of OH mass fraction presented below.

As we can see on fig. 4, similarly to the results for RMS of velocity fluctuations, the RMS of mixture fraction is hardest to predict correctly close to the centerline, for $r < 10mm$, where the present simulation overpredicts the experimental data in the middle axial locations $x/D_B = 0.9, 1.3$; our results also underpredict the peak RMS at $x/D_B = 2.4$, but are still in much better agreement than Liu et al.'s calculation, for which the location of peak RMS has shifted to the centerline.

Figure 5 shows radial profiles of Favre-averaged temperature. Here, we can see the effect of the temperature boundary condition on the bluff-body face: with the imposed experimentally measured temperature of $953K$, the temperature profiles at the upstream locations of $x/D_B = 0.26, 0.6$ are in much better agreement with experimental data, whereas without it the experimental data is overpredicred, by as much as $200K$ at $x/D_B = 0.6$. It can be seen that the present calculation (with the Dirichlet temperature boundary condition) compares favorably to other computational results. In particular, the simulation of Merci et al. considerably overpredicts (by roughly $250K$) the peak temperature values at $x/D_B = 0.6$, whereas that of Raman et al. underpredicts them (again, by about $250K$) at $x/D_B = 0.9, 1.3$. The calculations of Liu et al. are in good agreement with the experimental data up to $x/D_B = 1.3$, but for the last two axial locations the location of the peak in the radial profile is shifted towards the centerline.

We note that there is still considerable room for improvement in the present results. In particular, the temperature profiles at $x/D_B = 0.9, 1.3$ have large gradients near $r = 15mm$, unlike the experimental data and the other calculations. Also, at the upstream locations $x/D_B = 0.26, 0.6, 0.9$, the drop of the temperature profile from its peak to the coflow value is slower than that of experimental data and the other calculations, most likely due to the the more gradual drop in mean mixture fraction mentioned earlier. Therefore, it is expected that the agreement with experiment will be improved further by increased grid resolution at the outer shear layer.

Radial profiles of Favre-averaged CO mass fraction are shown on fig. 6. Here again, we can see the slower decrease in our simulation from the peak to the coflow value past $r = 25mm$. Also, at $x/D_B = 2.4$ the peak of CO mass fraction is shifted from $r = 10mm$ in the experimental data to $r = 5mm$, but the present results are still in better agreement at that location than those of Liu et al., which is the only other computational study to report mass fractions at that location. Upstream, at $x/D_B = 0.26$, both our simulation and that of Liu et al. are in good agreement with the peak CO mass fraction, whereas the calculation of Raman et al. underpredicts it by about 1% mass fraction; from here on, when discussing differences in mass fraction values, we shall use

the abbreviation MF to denote absolute values. For example, if we have an experimental value is 8%MF, and a computed value is 6%MF, we will either say that the computed value underpredicts experiment by 2%MF, or that it underpredicts experiment by 25%, the latter denoting relative differences.

Figure 7 shows radial profiles of Favre-averaged CO_2 mass fraction. The LES/HPDF calculation is generally in good agreement with the experiment, although the peak of the profile is consistently underpredicted by about 0.5%MF. Except at $x/D_B = 0.26$ and $x/D_B = 1.8$, where Raman et al.'s simulation better predicts the peak mass fraction, the current simulation gives an improvement over previous results.

Radial profiles of NO are shown on figure 8. Here we see some overprediction of the experimental results in both our simulation, but the agreement with experimental data is a condierable improvement over that of Liu et al. At the first four upstream locations, the present simulation reduces the overprediction of Liu et al.'s, approximately by half. At the two downstream locations, both computational profiles match experiment for $r > 15mm$, but for $r < 15mm$ the present simulation is considerably closer to the experimental profile than Liu et al.'s simulation. It is not surprising that this trend is similar to what was seen on the temperature profiles on figure 5, since NO formation is greater at higher temperatures.

Finally, fig. 9 gives radial profiles of Favre-averaged OH mass fraction. We see good agreement with experiment at most locations, with the exception of $x/D_B = 0.6$, where the present calculation gives a profile which is more spread out, and underpredicts the peak OH mass fraction by 0.6%MF. On the other hand, the agreement with experimental data for $x/D_B = 0.26$, $r < 17mm$ is much better than that of the other two simulations for which data are available, and downstream, at $x/D_B = 1.3, 1.8, 2.4$, the agreement of our simulation and that of Raman et al. is much better than that of Liu et al.

Figures 10 and 11 show, for the axial locations $x/D_B = 0.6, 0.9$ and $x/D_B = 1.3, 1.8$ respectively, scatter plots of temperature vs. mixture fraction, for the mixture fraction interval $\xi \in [0, 0.2]$ which includes the stoichiometric value of $\xi = 0.052$. For the reader's reference, a laminar flamelet profile is also shown, calculated via CHEMKIN's OPPDIF module, using the ARM2 chemical mechanism and a strain rate of $30s^{-1}$. Note that there appears to be local extinction at the location $x/D_B = 0.6$. This is in fact inert mixing in the outer shear layer, as pointed out by Liu et al.: for the LES/HPDF calculation, all the data points in the low temperature band lie in the region $r/R_B > 0.94$. The agreement of the LES/HPDF conditional means to those of the experiment is good, with the exception that the present simulation does not capture the sharp decrease in the conditional mean between the stoichiometric point and $\xi = 0.07$. We should note that Liu et al. [12], and Merci et al. [13] also provide temperature scatter plots at some of these locations, which cannot be reproduced for comparison here.

Contour plots of resolved axial velocity and temperature (with and without the temperature Dirichlet boundary condition) at the end of the simulation are provided on figures 12, 13, and 14 respectively. Due to the hydrodynami-

cally complex nature of the bluff-body flow, with vortex shedding at both shear layers, we can see that the instantaneous velocity and temperature fields are considerably more complex than what is suggested by the Favre-averaged radial plots. Also, a comparison of figures 13 and 14 illustrates the significant effect of the bluff-body temperature boundary condition on the upstream temperature field.

4.2 Results for Flame HM2

In this subsection, we present results for flame HM2, and make a comparison with experimental data and the calculations of Liu et al. and Merci et al.

A comparison of mean and RMS mixture fractions can be seen on figures 15 and 16, respectively. Similarly to the HM1 case, the LES/HPDF mean mixture fraction is generally in good agreement with experiment, again with the exception of a slower decrease to the coflow value past $r = 25mm$ and some underprediction of the experimental data for $x/D_B = 1.8, 2.4$, $r < 10mm$. In contrast, the calculations of Liu et al. considerably underpredict the mean mixture fraction at $x/D_B = 1.8, 2.4$, and overpredict it close to the bluff-body face, ar $x/D_B = 0.26$, $5mm < r < 25mm$. The calculations of Merci et al. give better agreement with experiment than those of Liu et al., but not as good as the LES/HPDF simulation: the peak values at the centerline are overpredicted, and the profile is less spread out in the radial direction for $x/D_B = 1.8$.

On the RMS mixture fraction plots (fig. 16), we again see that the largest differences between simulations and experiment are in the peak RMS values close to the centerline. These are well captured by the LES/HPDF calculation and that of Merci et al. (though in the latter, the peak at $x/D_B = 1.8$ is closer to the centerline than in the experiment), and considerably overpredicted by the simulation of Liu et al.

Radial profiles of Favre-averaged temperature are shown on fig. 17. On the two upstream plots of $x/D_B = 0.26$ and 0.6 we see that the LES/HPDF profile is in good agreement with experimental data, whereas the two RANS/PDF simulations of Liu et al. and Merci et al. underpredict temperature by as much as $200K$. At $x/D_B = 0.9$ and 1.3, the agreement between LES/HPDF and experiment is somewhat poorer, with the location of the peak temperature closer to the centerline. Downstream, at $x/D_B = 1.8$ and 2.4 there is again good agreement with experiment, particularly when compared to the simulation of Liu et al., which considerably overpredicts the experimental profile. We note again the presence in the LES/HPDF simulations of the artifacts seen in the HM1 results, namely a slower decrease of the profile past $r = 25mm$ for the upstream locations, and a high gradient near $r = 10mm$ for the $x/D_B = 0.9$ profile.

Figure 18 shows radial profiles of mean CO mass fraction. Here, we see that both simulations - LES/HPDF and that of Liu et al. - are in good agreement with experimental data, except at $x/D_B = 1.8$, where the results of Liu et al. considerably overpredict the CO mass fraction close to the centerline.

Radial profiles of the mean CO_2 mass fraction are shown on fig. 19. Similarly

to the HM1 case, the LES/HPDF similation is in good agreement with the experiment - the peak mass fraction is underpredicted by about 1%MF at the first three locations, and overpredicted by approximately 0.5%MF at $x/D_B = 1.3$ and $x/D_B = 1.8$. This trend (underprediction upstream, overprediction downstream) is more pronounced in the simulation of Liu et al., but the agreement of that calculation with experiment is better here than in the HM1 case.

Mean NO mass fraction profiles are shown on fig. 20. The most significant difference from the results for the HM1 case is that both simulations accurately predict the experimental results at $x/D_B = 0.26$. Similarly to the HM1 case, at the $x/D_B = 0.6$ and $x/D_B = 0.9$ locations, the LES/HPDF simulation somewhat overpredicts experimental results, by up to 20% of the experimental value, and this discrepancy is doubled in the Liu et al. simulation. Downstream, LES/HPDF provides a considerable improvement over the results of Liu et al., which are significantly higher than the experiment close to the centerline.

Finally, OH mass fractions are shown on fig. 21. Here, we see that for the upstream locations $x/D_B = 0.26, 0.6$ and 0.9, the LES/HPDF profiles correctly capture the peak OH mass fractions, but are more spread out in the radial direction, and again, the decrease past $r = 25mm$ is slower. For those locations, Liu et al.'s results give better agreement with experiment. The opposite is true of the downstream locations $x/D_B = 1.8$ and 2.4 where LES/HPDF simulations correctly capture the location of peak OH mass fraction, whereas the calculations of Liu et al. predict a peak closer to the centerline.

Scatter plots of temperature vs. mixture fraction are shown on figures 22 and 23, for the axial locations $x/D_B = 0.6, 0.9$ and $x/D_B = 1.3, 1.8$ respectively. At $x/D_B = 0.6$, the temperature variation near the stoichiometric point is significantly lower in the LES/HPDF simulation than in the experiment, and the experimentally measured maximal temperatures (up to $2400K$) are considerably underpredicted - the LES/HPDF maximum is $2250K$. Apart from the location $x/D_B = 0.6$, the agreement of the LES/HPDF simulation with experimental data is good, both in the conditional means and in the fact that the present simulation features considerable local extinction at $x/D_B = 1.8$, similarly to the experimental data, though above $\xi = 0.1$ the lower bound of the experimental scatter plot is overpredicted by up to $150K$. Similarly to the HM1 case, the sharp decrease in the conditional mean from the stoichiometric point to $\xi = 0.07$ is not replicated in the LES/HPDF simulation.

4.3 Results for Flame HM3

In this subsection, we present results for flame HM3, and make a comparison with experimental data and the calculations of Liu et al. and Merci et al.

A comparison of mean and RMS mixture fractions can be seen on figures 24 and 25, respectively. Similarly to the HM1 and HM2 cases, the LES/HPDF mean mixture fraction is generally in good agreement with experiment, again with the exception of a slower decrease to the coflow value past $r = 25mm$ and some underprediction of experiment for $x/D_B = 1.8$ and 2.4, $r < 10mm$. Similarly to the HM2 case, Liu et al. considerably underpredict the mean mixture

fraction at $x/D_B = 1.8, 2.4$, and overpredict it close to the bluff-body face, ar $x/D_B = 0.26$, $5mm < r < 25mm$. The calculations of Merci et al. give better agreement with experiment than those of Liu et al., although the peak values at the centerline are overpredicted, and the profile is less spread out in the radial direction for $x/D_B = 1.8$.

On the RMS mixture fraction plots (fig. 25), we again see that the largest differences between simulations and experiment are in the peak RMS values close to the centerline. These are well captured by the LES/HPDF calculation and that of Merci et al. (again, the peak at $x/D_B = 1.8$ is closer to the centerline than experiment), and considerably overpredicted by the simulation of Liu et al.

Radial profiles of Favre-averaged temperature are shown on fig. 26. On the upstream plot of $x/D_B = 0.26$ we see that the LES/HPDF profile underpredicts the experimental data, but is in better agreement than the calculations of Liu et al. At $x/D_B = 0.6$ both LES/HPDF and the calculations of Liu et al. are in good agreement with experiment, whereas Merci et al. underpredict the temperature profile by as much as $400K$. In the two intermediate axial locations LES/HPDF and Liu et al. are again in good agreement with experiment. The profile of Liu et al. becomes more inaccurate downstream, and overpredicts experiment by as much as $600K$ at $x/D_B = 2.4$. Unlike in the HM1 and HM2 cases, the LES/HPDF profile, too, loses some of its accuracy downstream, overpredicting the peak temperature value by $100K$ at $x/D_B = 1.8$ and by $150K$ at $x/D_B = 2.4$. Still, the agreement with experiment is much better than that of the RANS/PDF simulations.

Figure 27 shows radial profiles of mean CO mass fraction. Here, we see that both simulations - LES/HPDF and that of Liu et al. - are in good agreement with experimental data downstream, except at $x/D_B = 1.8$, where the results of Liu et al. considerably overpredict the CO mass fraction close to the centerline. At the two upstream locations, the LES/HPDF simulation overpredicts experimental data by as much as 1%MF, but is still considerably more accurate than the simulation of Liu et al., which overpredict experiment by as much as 5%MF.

Mean CO_2 mass fraction profiles are shown on figure 28. At $x/D_B = 1.3$ and downstream from that location, the results are similar to the HM1 and HM2 cases - LES/HPDF slightly overpredicts the experimental profile, by up to 10% of the experimental values, whereas Liu et al. are in good agreement with experiment for for $r > 10mm$ but considerably overpredict experimental values close to the centerline. At the three upstream locations, particularly at $x/D_B = 0.26$, the agreement, for both the present simulation and Liu et al., is poorer than in the HM1 and HM2 cases: in particular, the LES/HPDF simulation underpredicts experiment by up to 1%MF at $x/D_B = 0.26$. Still, the present results for the most part predict experimental data better than those of Liu et al.

Figure 29 shows radial profiles of mean NO mass fractions. Again, the agreement of the LES/HPDF simulation with experimental data is poorer than that in the HM1 and HM2 cases, with the computational values overpredicting ex-

periment by a factor of more than 2 downstream. Still, there is an improvement over the previous RANS calculation, especially at $x/D_B = 0.6$ and $x/D_B = 0.9$ where, unlike in the HM1 and HM2 cases, Liu et al.'s calculation overestimates experimental results by more than a factor of 2.

Radial profiles of mean OH mass fractions are shown on fig. 30. Again, the agreement of the LES/HPDF results with experiment is not as good as in the HM1 and HM2 cases, particularly at $x/D_B = 1.8, 2.4$ where the LES/HPDF profile overpredicts the peak OH mass fraction, but is considerably better than that of Liu et al.'s profiles, especially at $x/D_B = 0.26$ where the latter profile considerably underpredicts the OH mass fraction for $r < 20mm$.

Scatter plots of temperature vs. mixture fraction are shown on figures 31 and 32, for the axial locations $x/D_B = 0.6, 0.9$ and $x/D_B = 1.3, 1.8$ respectively. Similarly to the HM2 case, the maxima on the temperature scatter plot for $x/D_B = 0.6$ are underpredicted in the LES/HPDF simulation, although the discrepancy at the stoichiometric point is not quite as pronounced. We can observe significant local extinction at $x/D_B = 0.9, 1.3$ and 1.8. The agreement in the conditional means is good at $x/D_B = 0.6$ and $x/D_B = 0.9$, but deteriorates somewhat at $x/D_B = 1.8$, where the LES/HPDF conditional means around $\xi = 0.07$ overpredict experiment by up to $100K$, and the local extinction is somewhat underpredicted. We note that experimental conditional means are not shown for $x/D_B = 1.3$ because they are not present in the experimental data set.

4.4 Further discussion

From the results presented in the above two subsections, we see that the LES/HPDF simulations of the flames HM1, HM2 and HM3 are in very good agreement with experiment, with the exception of the upstream locations past $r = 25mm$, where the LES/HPDF profiles decrease to the coflow values more slowly than the experimental data, most probably due to insufficient resolution in the outer shear layer. The LES/HPDF results are also a considerable improvement over other simulations of the same flames, especially at the downstream locations of $x/D_B = 1.8$ and 2.4.

As can be seen on the scatter plots of temperature vs. mixture fraction, the present simulation is able to capture the local extinction in the HM2 and HM3 cases, although the amount of local extinction is somewhat underpredicted in the downstream regions of the HM3 case. Nevertheless, the local extinction of flame HM3 is captured in the LES/HPDF calculation much better than in previous simulations: in particular, both the simulations of Liu et al. and the EMST simulations of Merci et al. considerably underpredict the amount of local extinction in the flames HM2 and HM3. For the flame HM2, another simulation reported in Merci et al., using a modified Curl's mixing model [13], yields scatter plots in better agreement with experimental data (in particular, the local extinction at $x/D_B = 1.8$ for the HM2 case is well-predicted), but gives more inaccurate mean field results, and cannot produce a stable burning solution for the HM3 case.

The consequences of the improved prediction of local extinction can be observed on figure 33, which plots the progression from flame HM1 to HM3, as given by experimental data, and as predicted by the present simulation and that of Liu et al. We can see that the experimental data indicates a sharp decrease in temperature at $x/D_B = 0.9$ from HM2 to HM3, as well as a progressive decrease in temperature from HM1 to HM2 to HM3 at the downstream locations $x/D_B = 1.3$, $x/D_B = 1.8$ and $x/D_B = 2.4$. These trends are approximated well by the LES/HPDF calculation, but not so much by that of Liu et al.

5 Conclusions

The Sandia-Sydney bluff-body flames have been simulated with a new LES/PDF algorithm, called LES/HPDF, developed by Cornell University's Turbulence and Combustion Group. Using the skeletal ARM2 chemical mechanism, the computational results are in very good agreement with experiment. A notable exception to this is in the outer shear layer close to the bluff-body, where the LES/HPDF-calculated scalars converge to the coflow value more slowly than experimental data and other computational results; additionally the NO mass fractions are generally overpredicted, especially downstream in the HM3 flame, but the agreement with experiment is still considerably better than in previous work. Overall, the present calculations are a substantial improvement on previous computational studies of the same flame, with better prediction of the local extinction in flames HM2 and HM3. It is seen that the simulation is sensitive to the treatment of heat transfer to the bluff body face, and better agreement of the temperature profiles with experiment is seen with the implementation of a Dirichlet temperature boundary condition which enforces the experimentally-observed mean temperature on the bluff-body face.

Acknowledgements

This work was supported by Office of Energy Research, Office of Basic Energy Sciences, Chemical Sciences, Geosciences and Biosciences Division of the US Department of Energy (DOE) under Grant DE-FG02-90ER-14128.

References

[1] S. B. Pope, *PDF Methods for Turbulent Reactive Flows*, Prog. Energy Combust. Sci., **11**, pp. 119-192 (1985)

[2] D. C. Haworth, *Progress in Probability Density Function Methods for Turbulent Reacting Flows*, Prog. Energy Comb. Sci., **36**, 2, (2010), pp. 168-259

[3] S. B. Pope *Computations of Turbulent Combustion: Progress and Challenges*, Proc. Comb. Inst., **23**, (1991), pp. 591-612

[4] S. B. Pope, *Turbulent Flows*, Cambridge University Press, Cambridge, 2000

[5] P. Colucci, F. Jaberi, P. Givi, and S. B. Pope, *Filtered Density Function for Large Eddy Simulation of Turbulent Reacting Flows*, Phys. Fluids **10** (1998), pp.499-515

[6] F. Jaberi, P. Colucci, S. James, P. Givi, and S. B. Pope, *Filtered Mass Density Function for Large Eddy Simulation of Turbulent Reacting Flows*, J. Fluid Mech. **401** (1999), pp.85-121

[7] Q. Tang, Ph.D. Thesis, Cornell University, 2003

[8] V. Raman, and H. Pitsch, *A Consistent LES/Filtered Density Function Formulation for the Simulation of Turbulent Flames with Detailed Chemistry*, Proc. Comb. Inst., **31**, (2007), pp. 1711-1719

[9] V. Raman, H. Pitsch, and R. O. Fox, *Eulerian Transported Probability Density Function Sub-Filter Model for Large-Eddy Simulations of Turbulent Combustion*, Comb. Theory Model., **10**, 3, (2006), pp. 439-458

[10] S. B. Pope *Self-Conditioned Fields for Large-Eddy Simulations of Turbulent Flows*, J. Fluid Mech., **652**, (2010), pp. 139-169

[11] A. R. Masri, and R. W. Bilger, *Turbulent Diffusion Flames of Hydrocarbon Fuels Stabilized on a Bluff Body*, Proc. Comb. Inst., **20**, (1985)

[12] K. Liu, S. B. Pope, and D. A. Caughey, *Calculations of Bluff-Body Stabilized Flames Using a Joint Probability Density Function Model with Detailed Chemistry*, Comb. Flame, **141**, (2005), pp. 89-117

[13] B. Merci, D. Roekaerts, B. Naud, and S. B. Pope, *Comparative Study of Micromixing Models in Transported Scalar PDF Simulations of Turbulent Nonpremixed Bluff Body Flames*, Comb. Flame, **146**, (2006), pp. 109-130

[14] A. Kempf, R. P. Lindstedt, and J. Janicka, *Large-Eddy Simulation of a Bluff-Body Stabilized Nonpremixed Flame*, Comb. Flame, **143**, (2006), pp. 170-189

[15] S. James, J. Zhu, M. Anand, and B. Sekar, *Large Eddy Simulations of Bluff-Body Stabilized Turbulent Flames and Gas Turbine Combustors*, DoD High Performance Computing Modernization Program Users Group Conference, Pittsburgh, PA, June 18-21

[16] V. Raman, H. Pitsch, and R. O. Fox, *Hybrid Large-Eddy Simulation/Lagrangian Filtered-Density-Function Approach for Simulating Turbulent Combustion*, Comb. Flame, **143**, (2005), pp. 56-78

[17] C. D. Pierce, and P. Moin, *Progress-Variable Approach for Large-Eddy Simulation of Turbulent Combustion*, J. Fluid Mech.**504**, (2004), pp. 73-97

[18] P. Moin, K. Squires, W. Cabot, and S. Lee, *A Dynamic Subgrid-Scale Model for Compressible Turbulence and Scalar Transport*, Phys. Fluids**3**, (1991), pp. 2746-2757

[19] M. Germano, U. Piomelli, P. Moin, and W.H. Cabot *A dynamic subgrid-scale eddy viscosity model*, Phys. Fluids, **3**, pp. 1760-1765, 1991

[20] R. O. Fox *Computational Models for Turbulent Reactive Flows*, Cambridge University Press, Cambridge, 2003

[21] S. Viswanathan, H. Wang, and S. B. Pope, *Numerical Implementation of Mixing and Molecular Transport in LES/PDF Studies of Turbulent Reacting Flows*, J. Comput. Phys. **230**, (2011), pp. 6916-6957

[22] H. Wang, and S. B. Pope *Large Eddy Simulation/Probability Density Function Modeling of a Turbulent $CH_4/H_2/N_2$ Jet Flame*, Proc. Comb. Inst., **33**, (2011), pp. 1319-1330

[23] P. P. Popov, H. Wang, and S. B. Pope, *Specific Volume Coupling and Convergence Properties in Hybrid Particle/Finite Volume Algorithms for Turbulent Reactive Flows*, J. Comp. Phys. (in review)

[24] J. Villermaux, and J.C. Devillon *Reprèsentation de la redistribution des domaines de sègrègation dans un fluide par un modèle d'interaction phènomènologique*, 2nd Int. Symp. Chem. React. Engng, Amsterdam, 1972

[25] S. B. Pope, *Computationally Efficient Implementation of Combustion Chemistry Using In Situ Adaptive Tabulation*, Comb. Theory Model., **1**, (1997), pp. 41-63

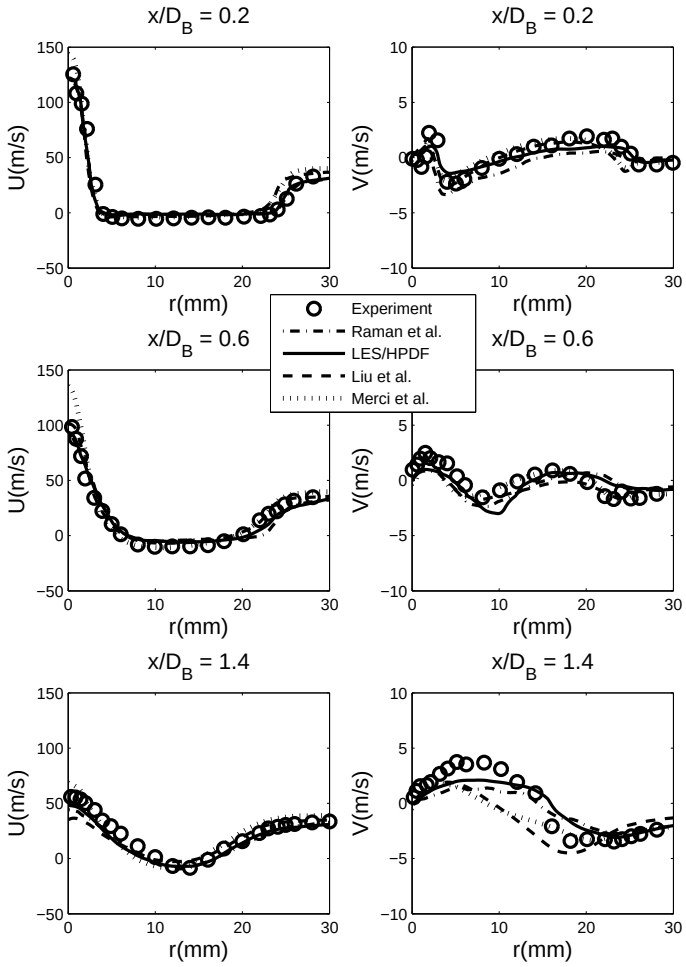

Figure 1: Mean velocity plots for the HM1e simulation. Left: radial plots of the Favre-averaged axial velocity at three different axial locations: $x = 0.2D_B, x = 0.6D_B$, and $x = 1.4D_B$. Right: plots of the Favre-averaged radial velocity at the same locations. As noted in the text, the LES/HPDF profiles are scaled by a factor of 108/118, in order to account for the velocity difference between flames HM1 and HM1e.

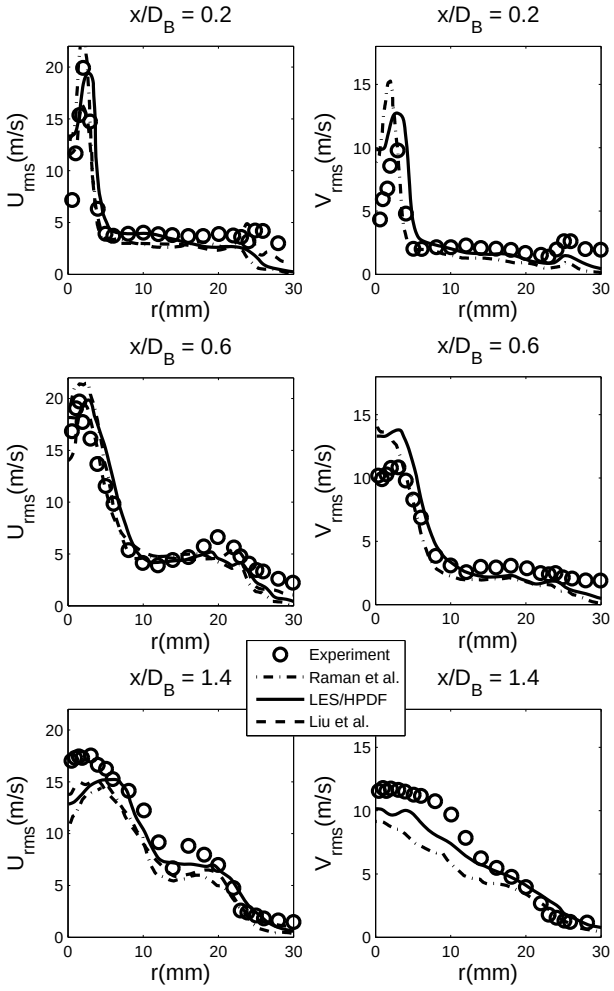

Figure 2: RMS velocity plots for the HM1e simulation. Left: radial plots of the root-mean-square of axial velocity fluctuations at three different axial locations: $x = 0.2D_B, x = 0.6D_B$, and $x = 1.4D_B$. Right: plots of the root-mean-square of axial velocity fluctuations at the same locations. As noted in the text, the LES/HPDF profiles are scaled by a factor of 108/118, in order to account for the velocity difference between flames HM1 and HM1e.

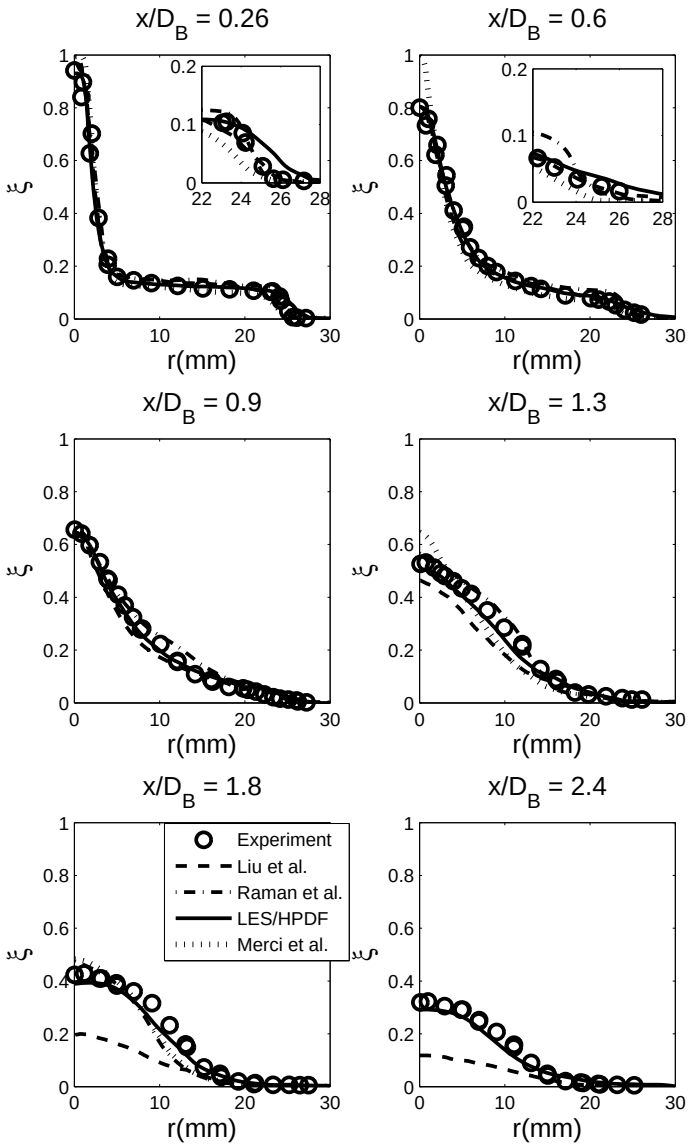

Figure 3: Radial plots of the Favre-averaged mixture fraction at six axial locations, from $x = 0.26D_B$ to $x = 2.4D_B$, for the HM1 simulation.

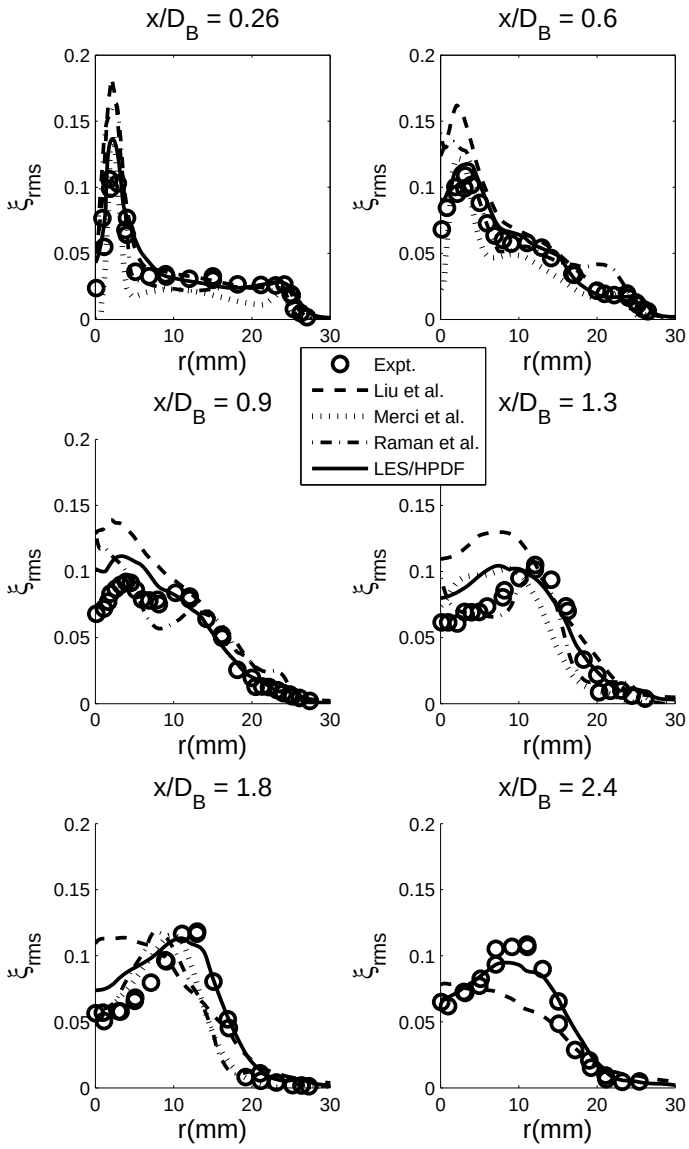

Figure 4: Radial plots of the root-mean-square of mixture fraction fluctuations at six axial locations, from $x = 0.26D_B$ to $x = 2.4D_B$, for the HM1 simulation.

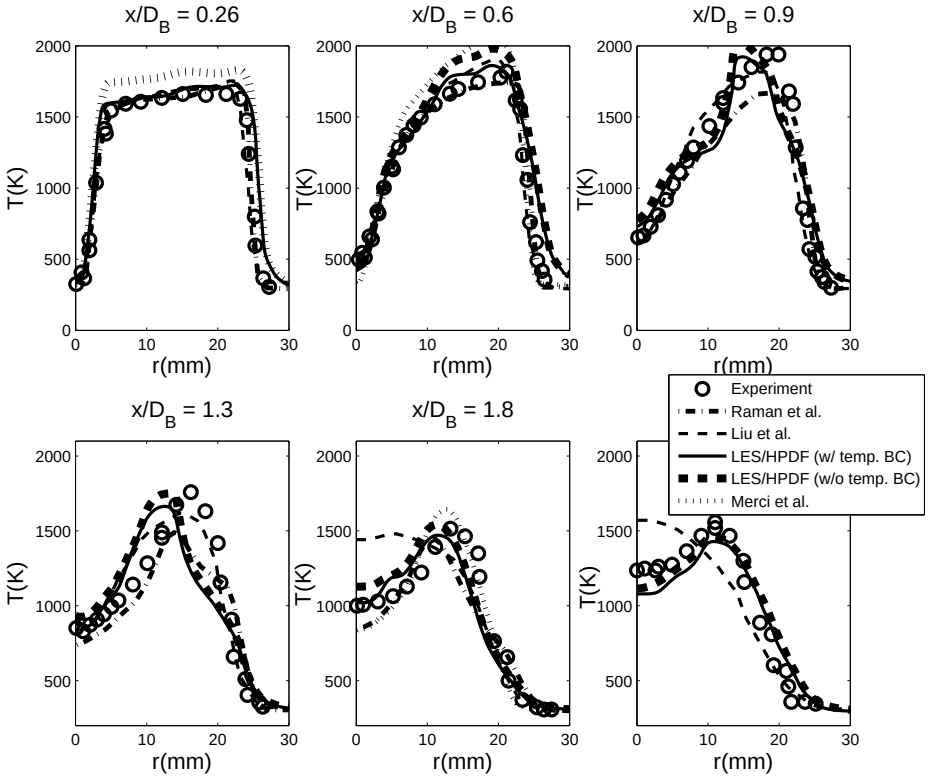

Figure 5: Radial plots of the Favre-averaged temperature at six axial locations, from $x = 0.26D_B$ to $x = 2.4D_B$, for the HM1 simulation, with and without the temperature boundary condition at the bluff-body face plate.

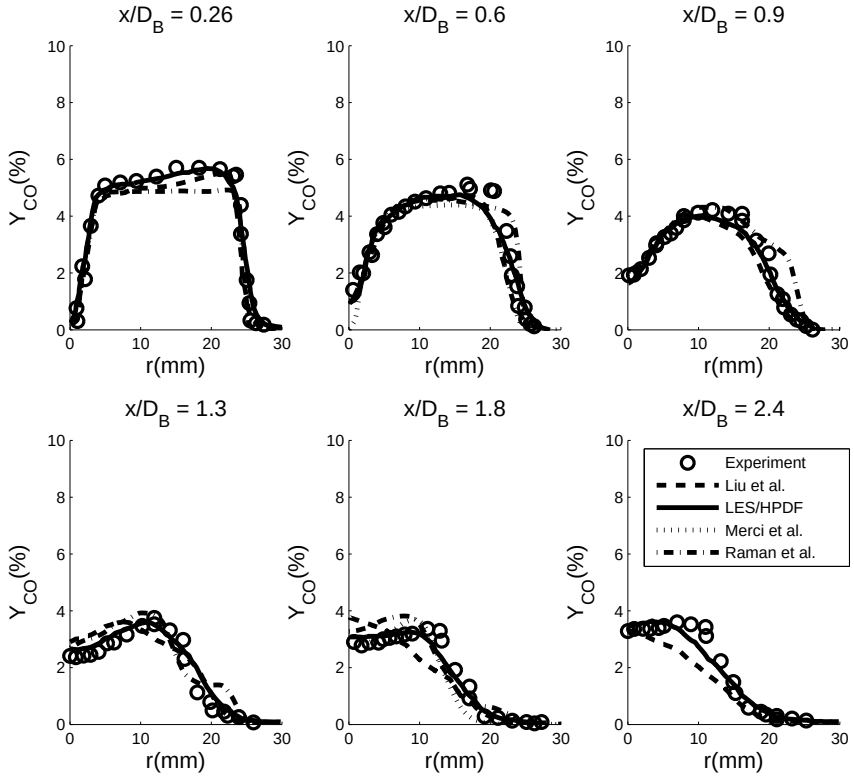

Figure 6: Radial plots of the Favre-averaged CO mass fraction at six axial locations, from $x = 0.26D_B$ to $x = 2.4D_B$, for the HM1 simulation.

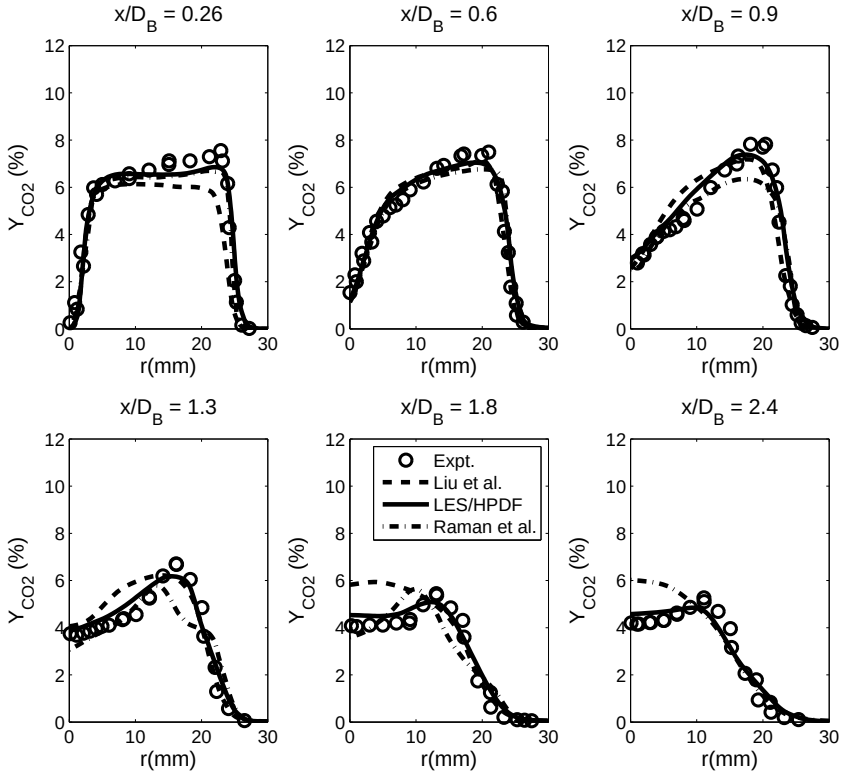

Figure 7: Radial plots of the Favre-averaged CO2 mass fraction at six axial locations, from $x = 0.26D_B$ to $x = 2.4D_B$, for the HM1 simulation.

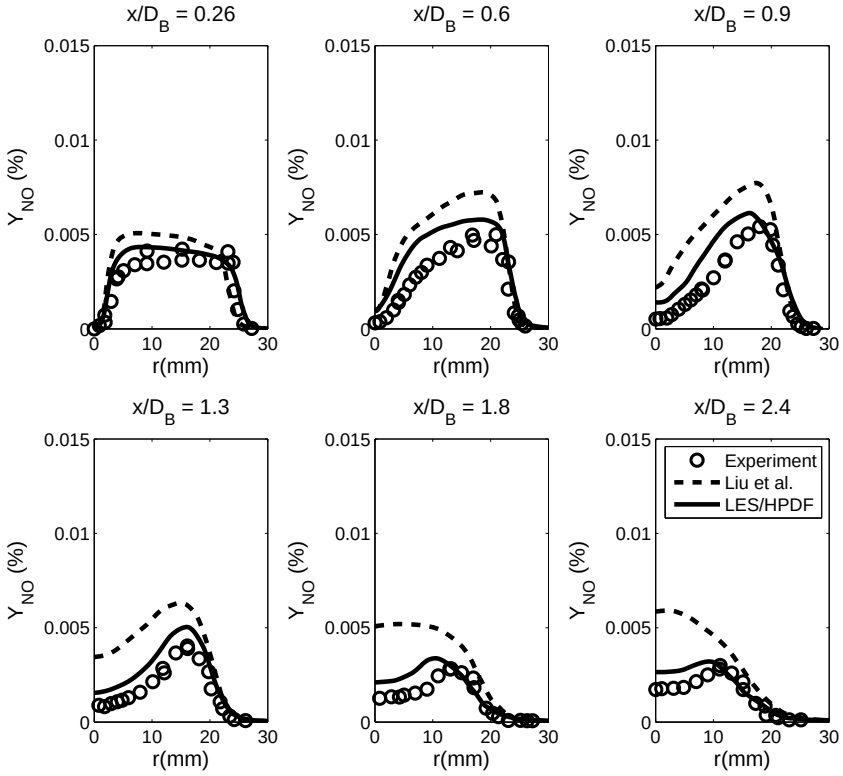

Figure 8: Radial plots of the Favre-averaged NO mass fraction at six axial locations, from $x = 0.26D_B$ to $x = 2.4D_B$, for the HM1 simulation.

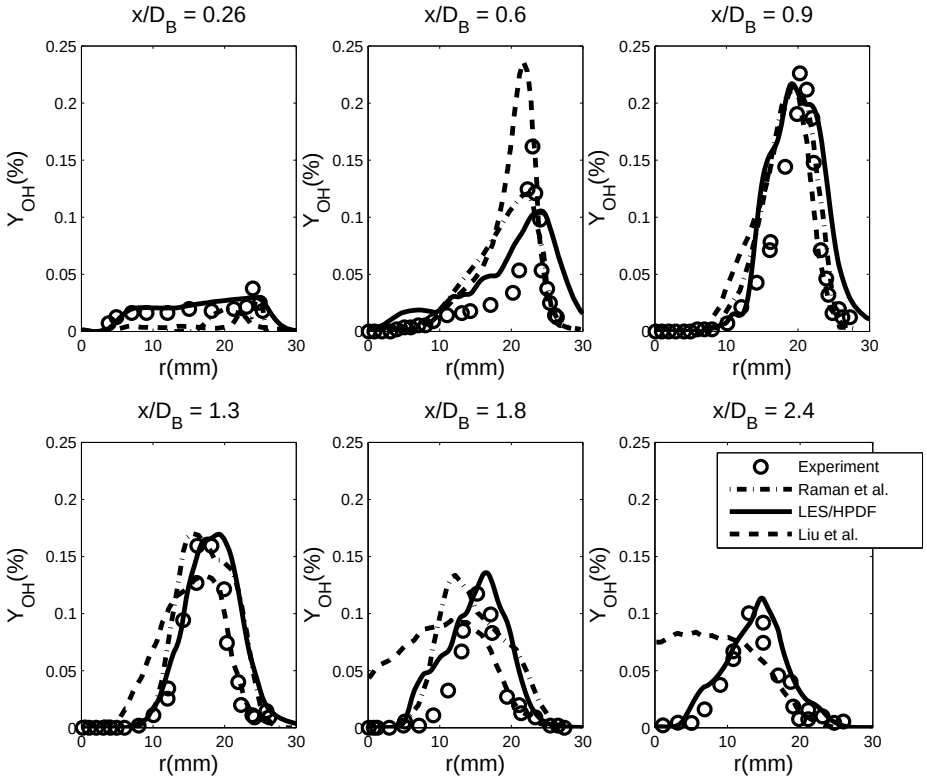

Figure 9: Radial plots of the Favre-averaged OH mass fraction at six axial locations, from $x = 0.26D_B$ to $x = 2.4D_B$, for the HM1 simulation.

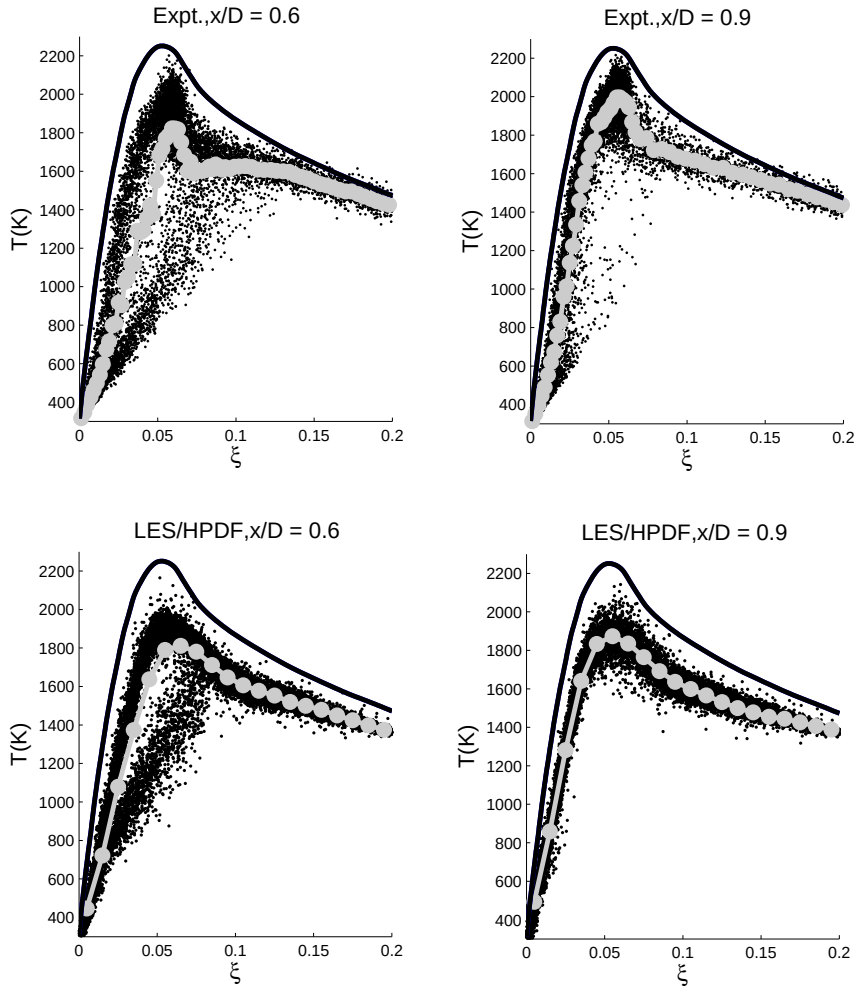

Figure 10: HM1 scatter plots of temperature plotted against mixture fraction, in the range $\xi \in [0, 0.2]$, for the axial locations $x = 0.6D_B$ and $x = 0.9D_B$. Conditional means are marked by the grey curve with circular symbols, and laminar flamelet temperatures are marked by the solid black curve. Top: experimental results. Bottom: LES/HPDF calculations.

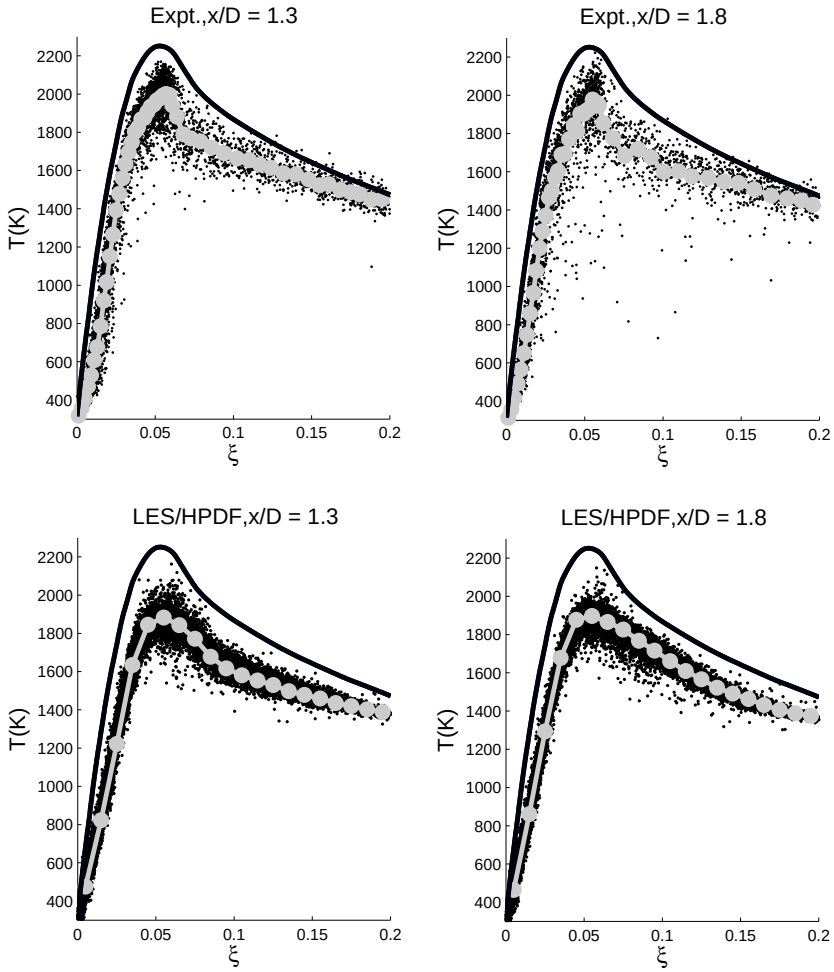

Figure 11: HM1 scatter plots of temperature plotted against mixture fraction, in the range $\xi \in [0, 0.2]$, for the axial locations $x = 1.3D_B$ and $x = 1.8D_B$. Conditional means are marked by the grey curve with circular symbols, and laminar flamelet temperatures are marked by the solid black curve. Top: experimental results. Bottom: LES/HPDF calculations.

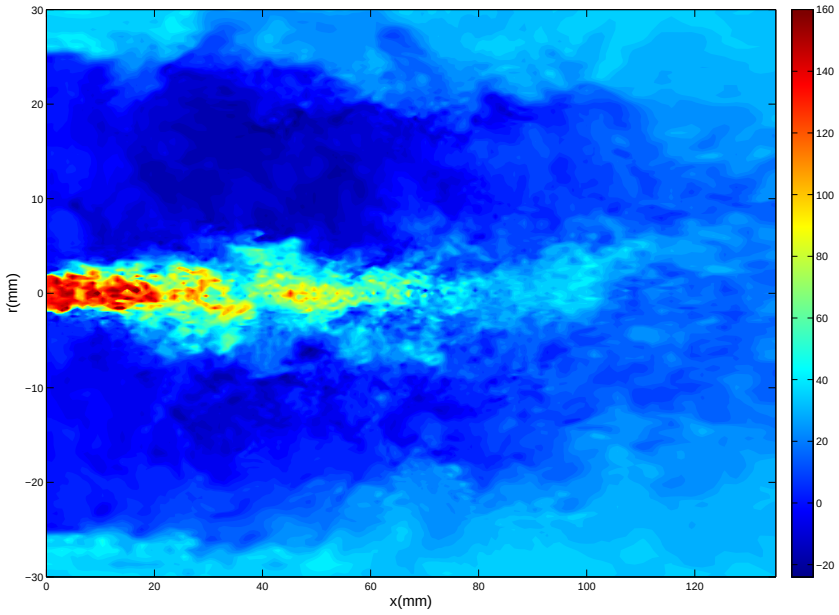

Figure 12: Contour plot of the resolved axial velocity (in m/s) at the end of the HM1 simulation.

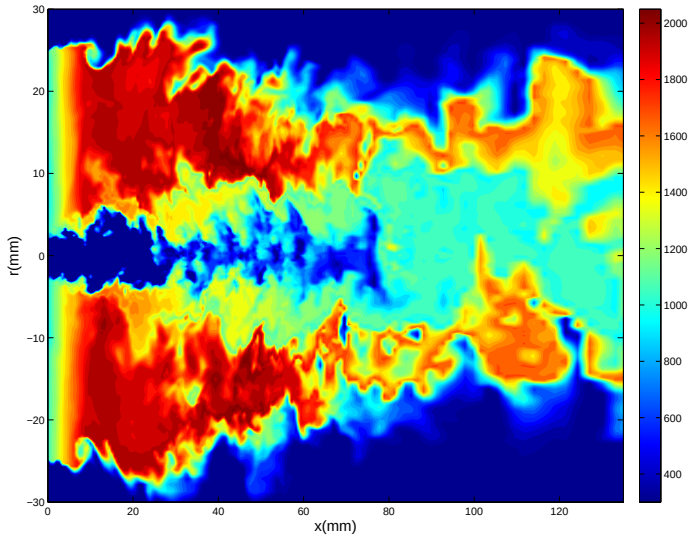

Figure 13: Contour plot of the resolved temperature (in K) at the end of the HM1 simulation, with a specified temperature at the bluff-body face.

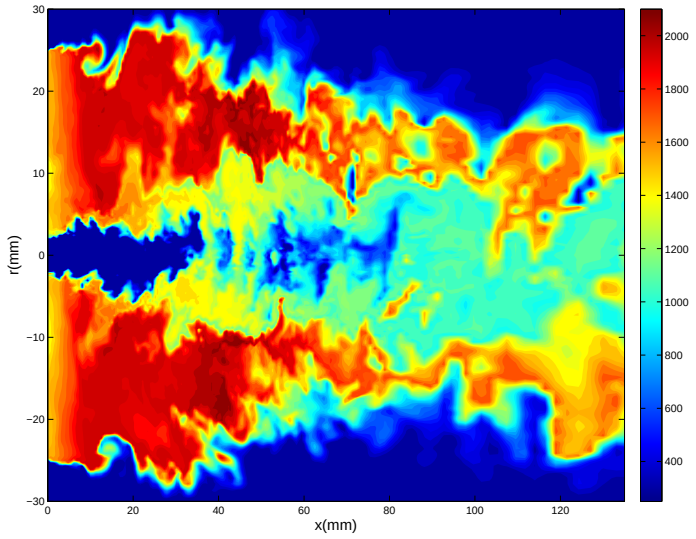

Figure 14: Contour plot of the resolved temperature (in K) at the end of the HM1 simulation, without the temperature boundary condition (bluff-body face is adiabatic).

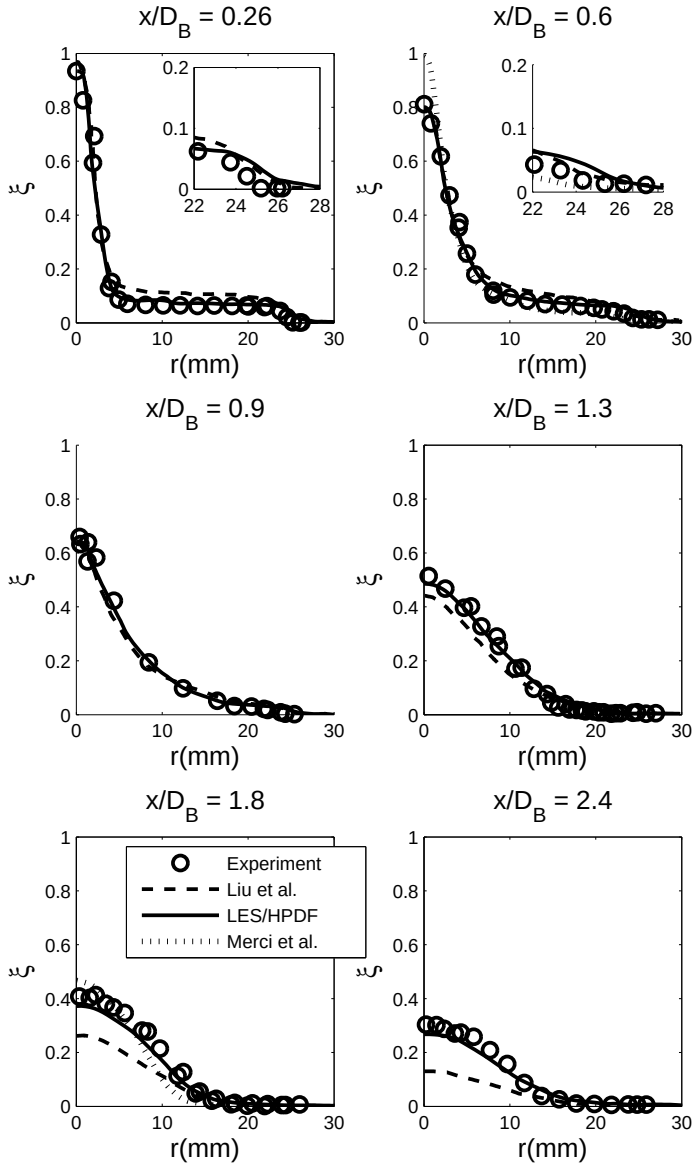

Figure 15: Radial plots of the Favre-averaged mixture fraction at six axial locations, from $x = 0.26D_B$ to $x = 2.4D_B$, for the HM2 simulation.

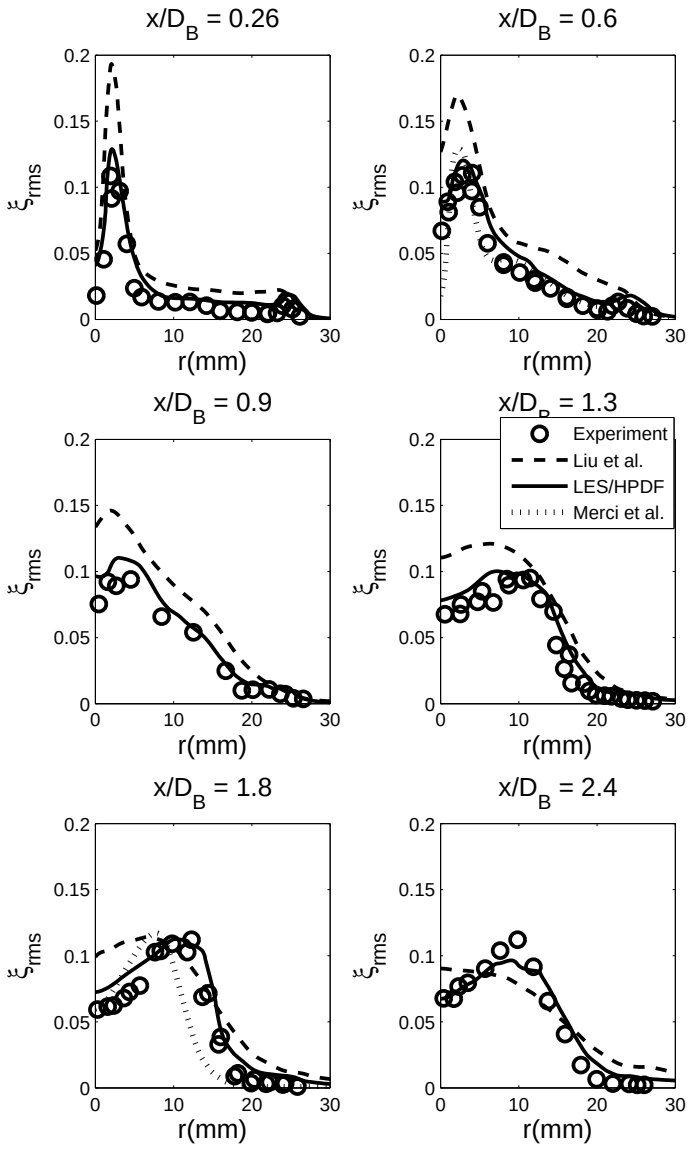

Figure 16: Radial plots of the root-mean-square of mixture fraction fluctuations at six axial locations, from $x = 0.26D_B$ to $x = 2.4D_B$, for the HM2 simulation.

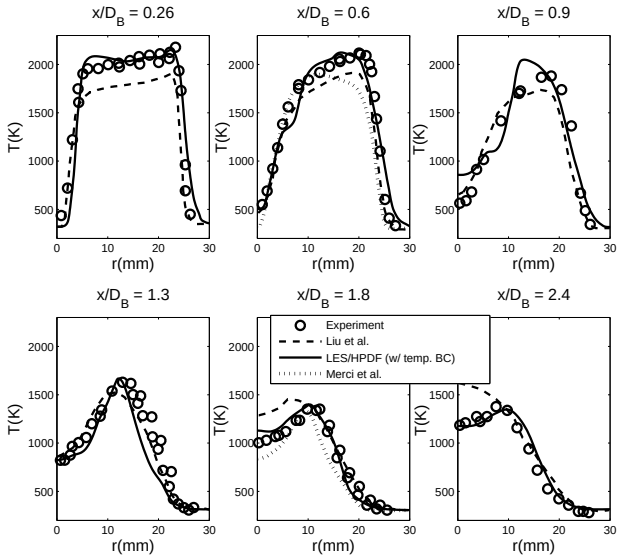

Figure 17: Radial plots of the Favre-averaged temperature at six axial locations, from $x = 0.26D_B$ to $x = 2.4D_B$, for the HM2 simulation.

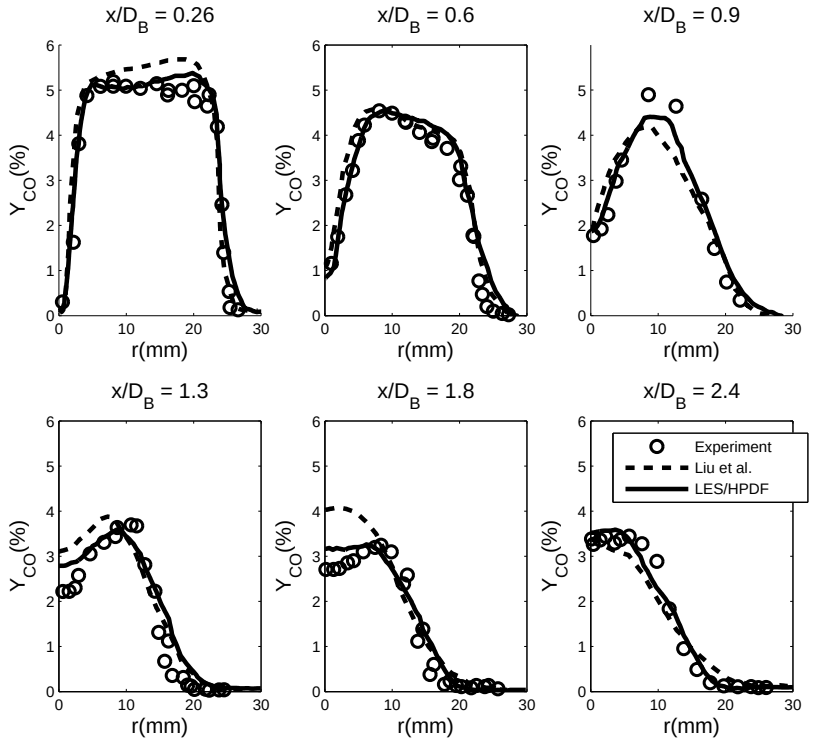

Figure 18: Radial plots of the Favre-averaged CO mass fraction at six axial locations, from $x = 0.26D_B$ to $x = 2.4D_B$, for the HM2 simulation.

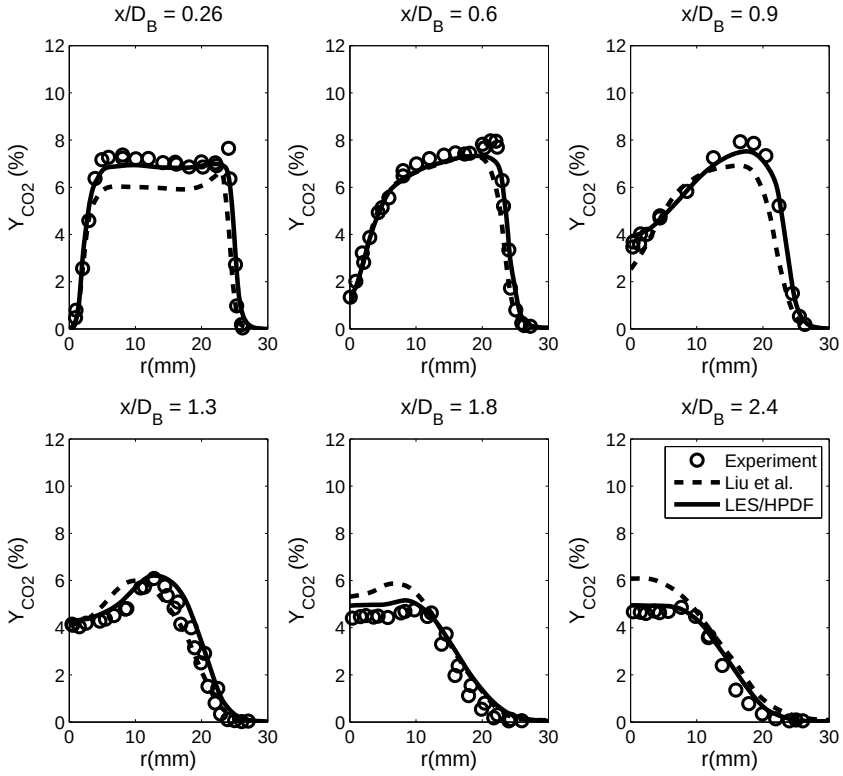

Figure 19: Radial plots of the Favre-averaged CO2 mass fraction at six axial locations, from $x = 0.26D_B$ to $x = 2.4D_B$, for the HM2 simulation.

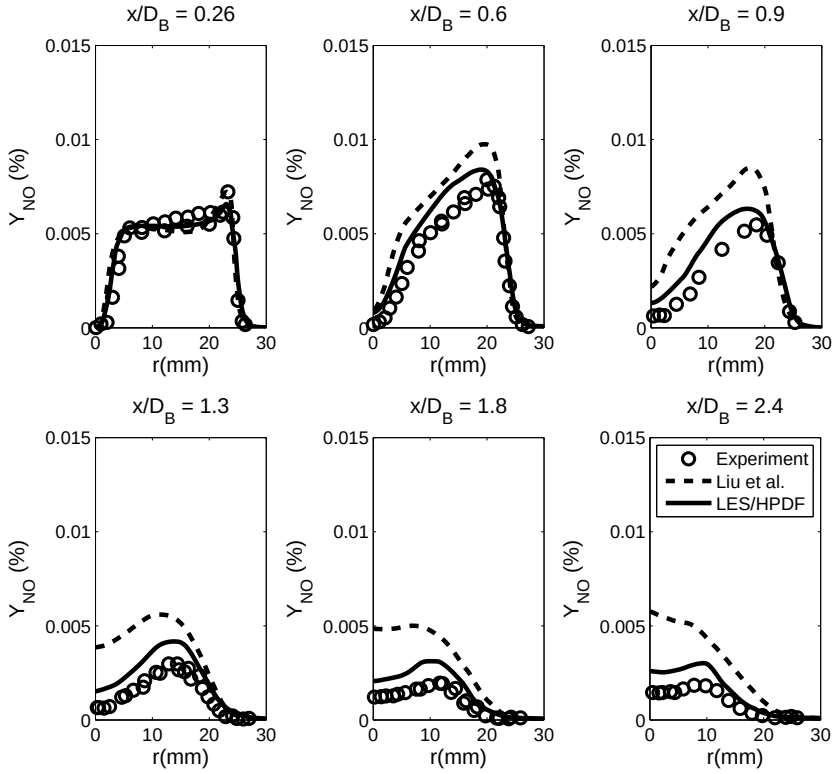

Figure 20: Radial plots of the Favre-averaged NO mass fraction at six axial locations, from $x = 0.26D_B$ to $x = 2.4D_B$, for the HM2 simulation.

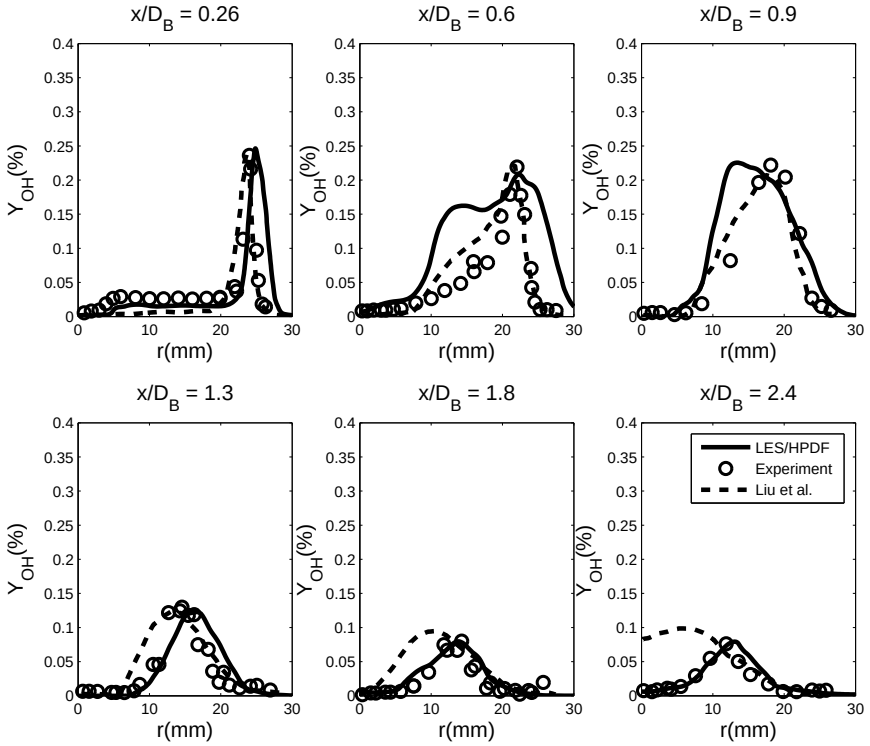

Figure 21: Radial plots of the Favre-averaged OH mass fraction at six axial locations, from $x = 0.26D_B$ to $x = 2.4D_B$, for the HM2 simulation.

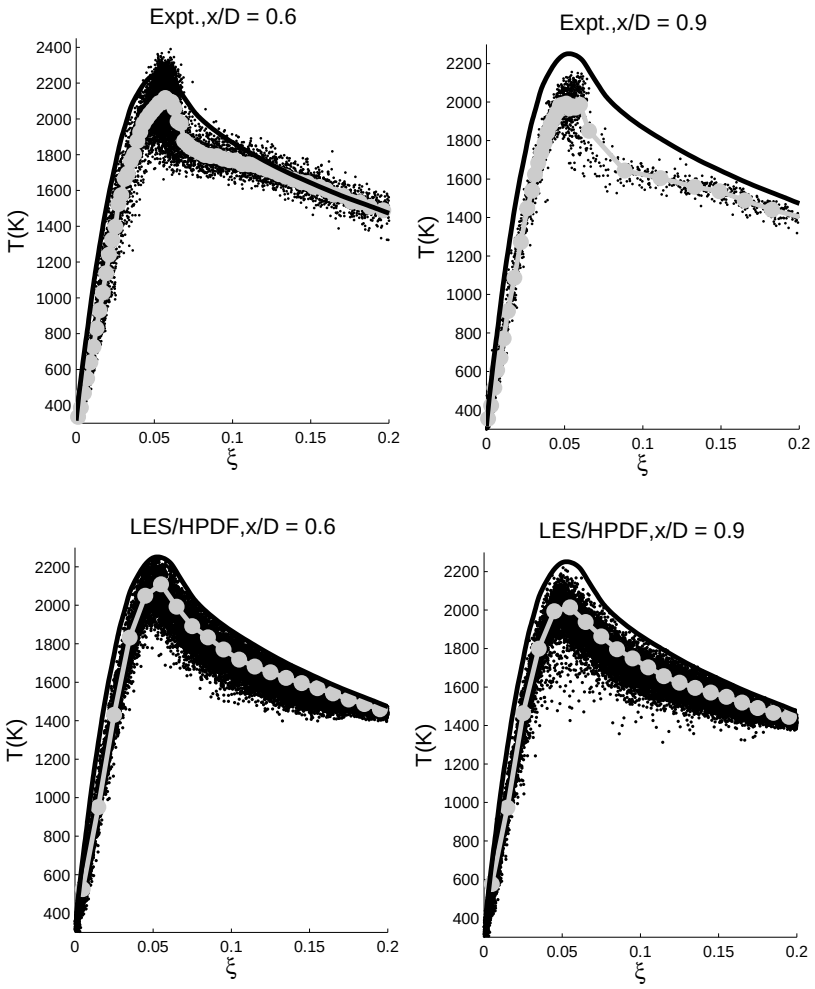

Figure 22: HM2 scatter plots of temperature plotted against mixture fraction, in the range $\xi \in [0, 0.2]$, for the axial locations $x = 0.6D_B$ and $x = 0.9D_B$. Conditional means are marked by the grey curve with circular symbols, and laminar flamelet temperatures are marked by the solid black curve. Top: experimental results. Bottom: LES/HPDF calculations.

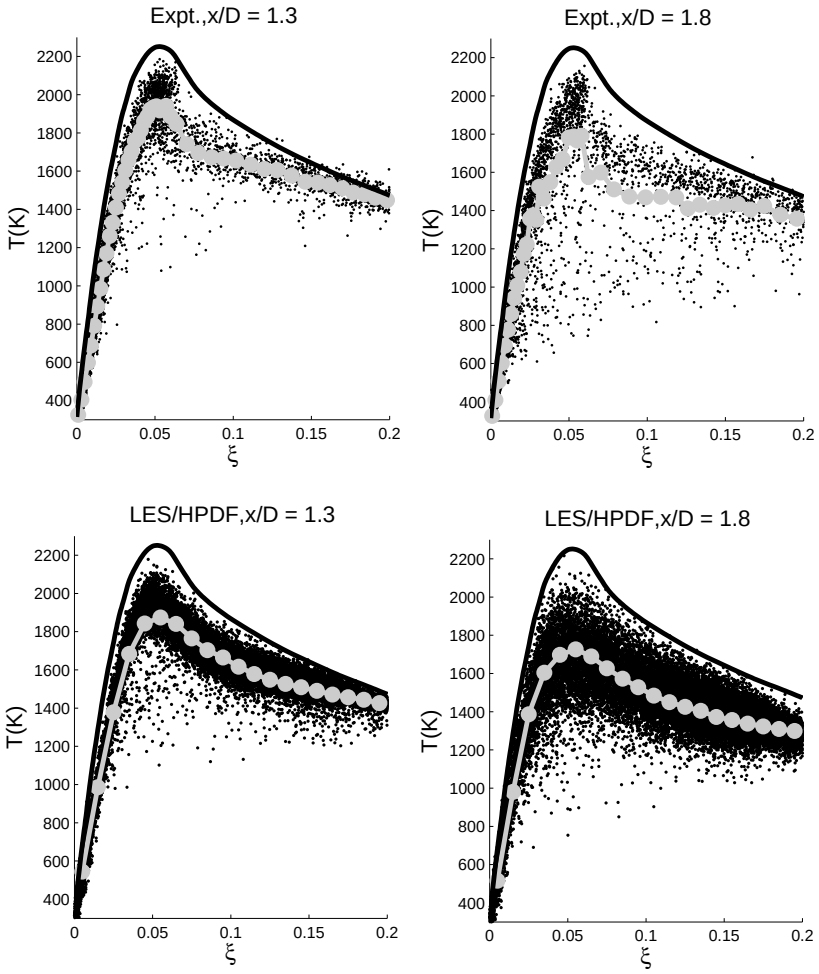

Figure 23: HM2 scatter plots of temperature plotted against mixture fraction, in the range $\xi \in [0, 0.2]$, for the axial locations $x = 1.3D_B$ and $x = 1.8D_B$. Conditional means are marked by the grey curve with circular symbols, and laminar flamelet temperatures are marked by the solid black curve. Top: experimental results. Bottom: LES/HPDF calculations.

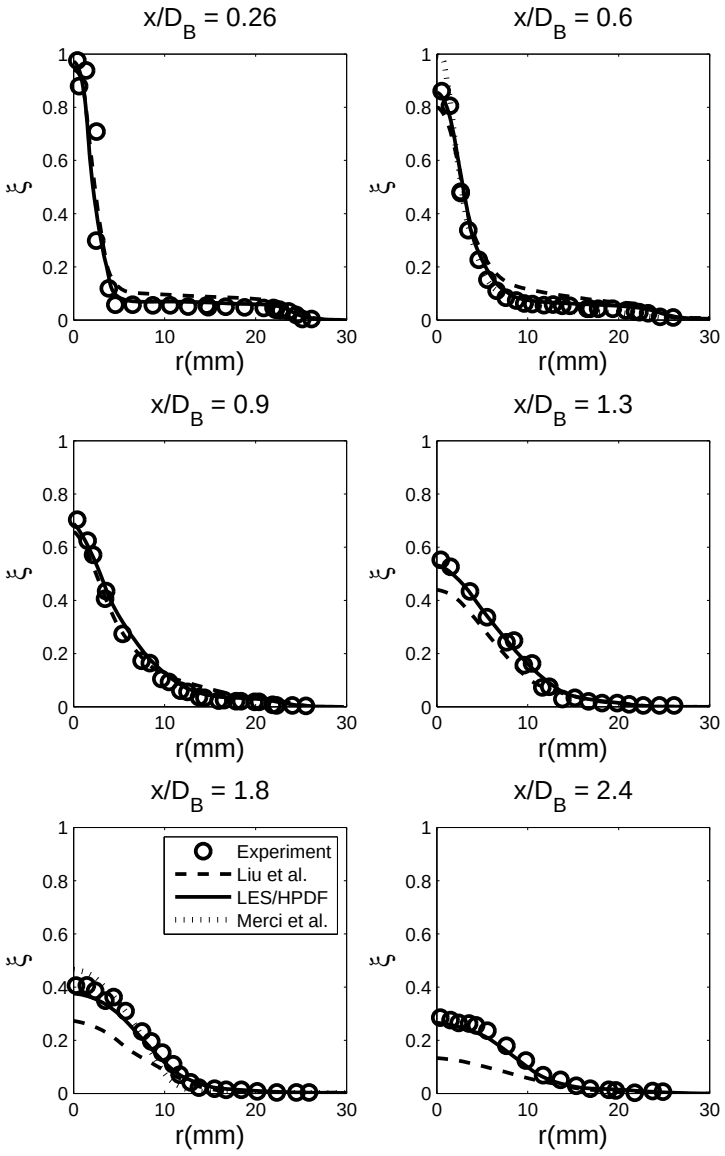

Figure 24: Radial plots of the Favre-averaged mixture fraction at six axial locations, from $x = 0.26D_B$ to $x = 2.4D_B$, for the HM3 simulation.

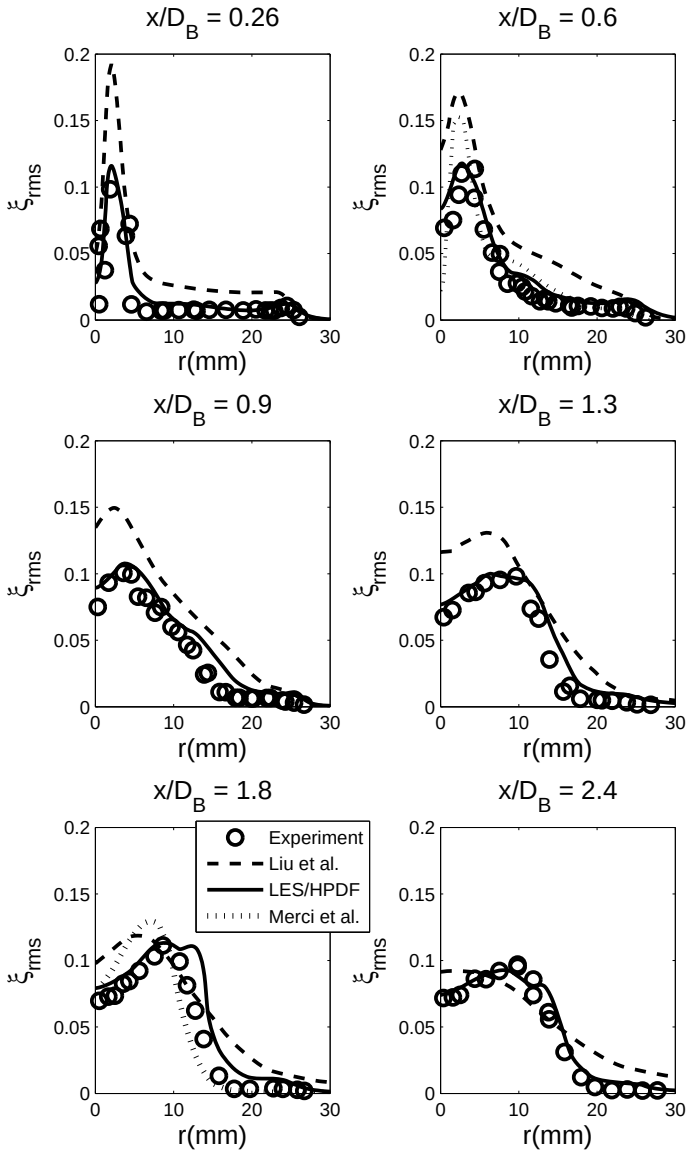

Figure 25: Radial plots of the root-mean-square of mixture fraction fluctuations at six axial locations, from $x = 0.26D_B$ to $x = 2.4D_B$, for the HM3 simulation.

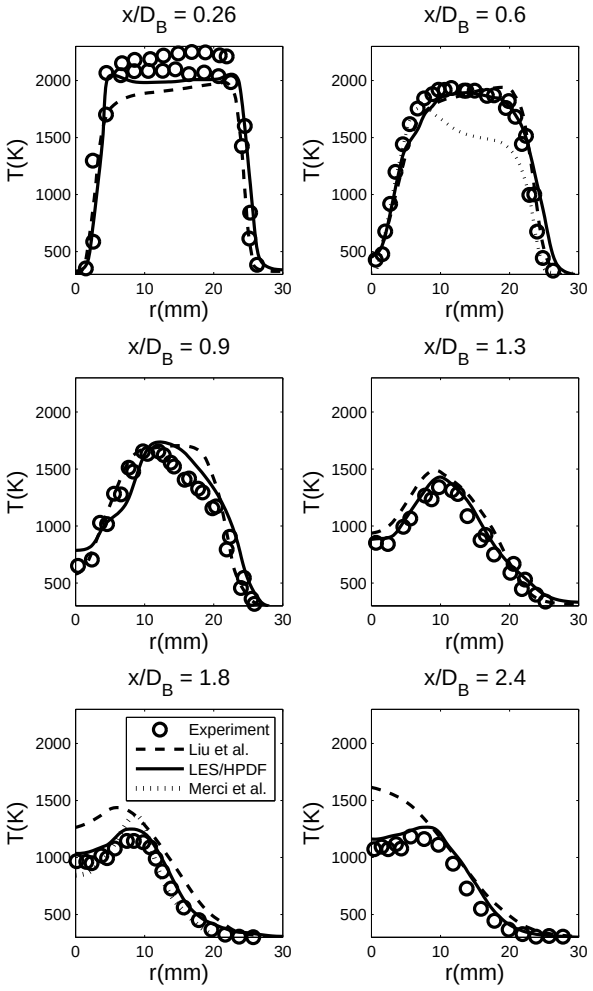

Figure 26: Radial plots of the Favre-averaged temperature at six axial locations, from $x = 0.26D_B$ to $x = 2.4D_B$, for the HM3 simulation.

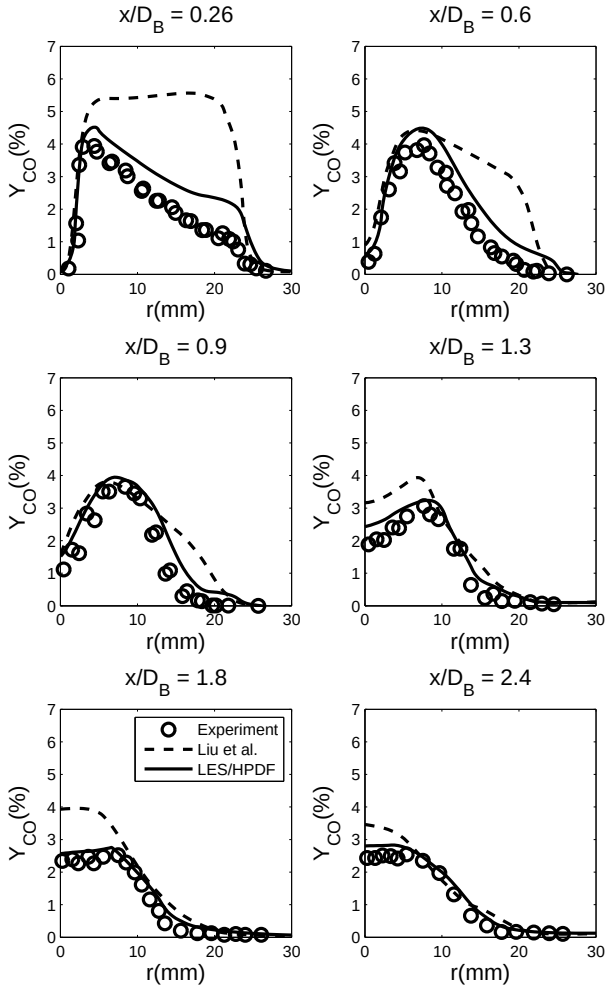

Figure 27: Radial plots of the Favre-averaged CO mass fraction at six axial locations, from $x = 0.26D_B$ to $x = 2.4D_B$, for the HM3 simulation.

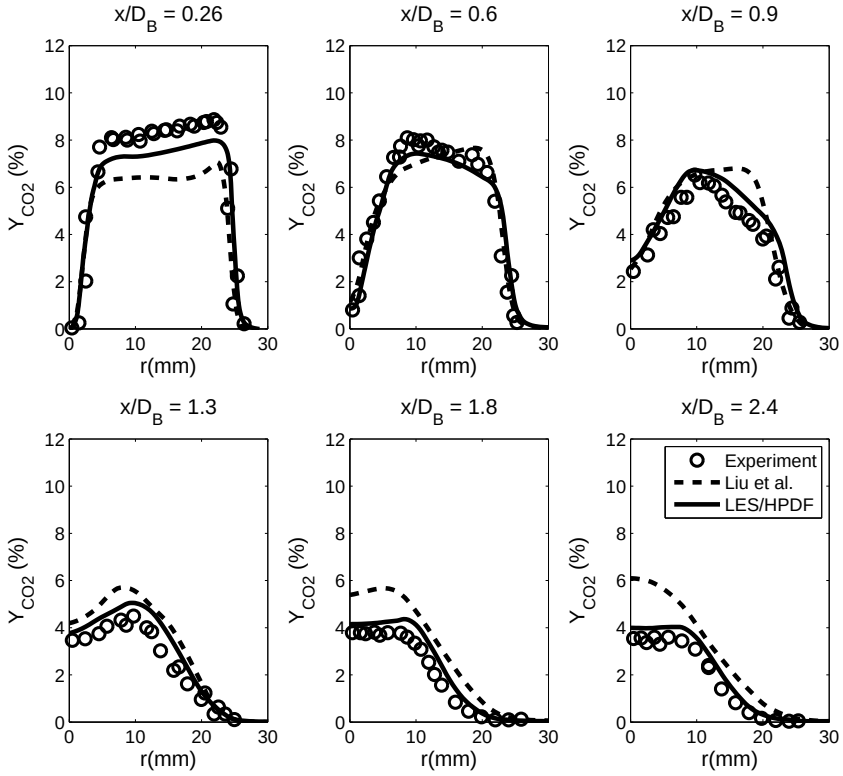

Figure 28: Radial plots of the Favre-averaged CO2 mass fraction at six axial locations, from $x = 0.26D_B$ to $x = 2.4D_B$, for the HM3 simulation.

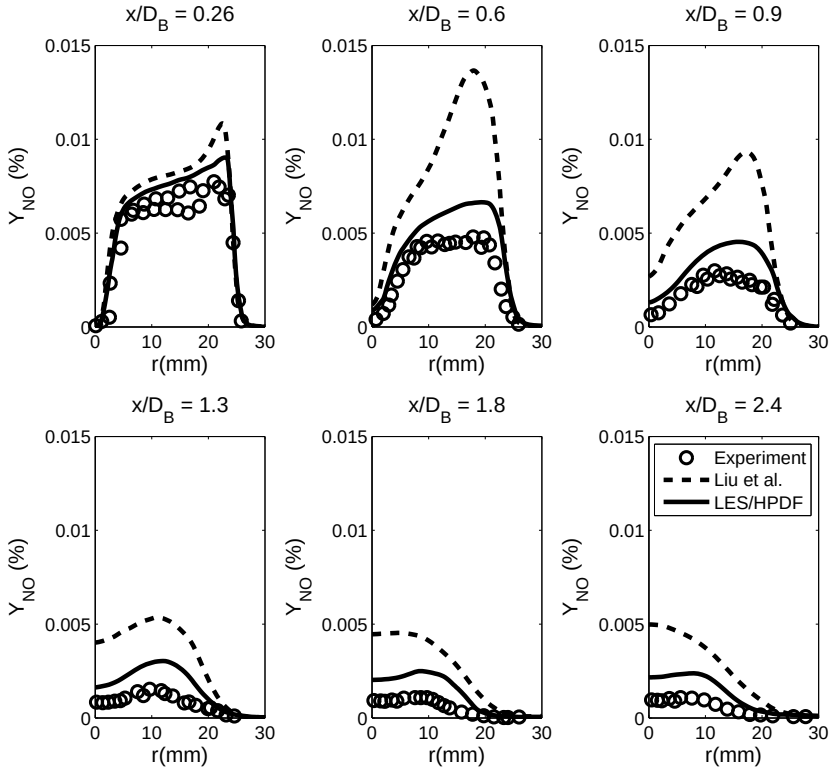

Figure 29: Radial plots of the Favre-averaged NO mass fraction at six axial locations, from $x = 0.26D_B$ to $x = 2.4D_B$, for the HM3 simulation.

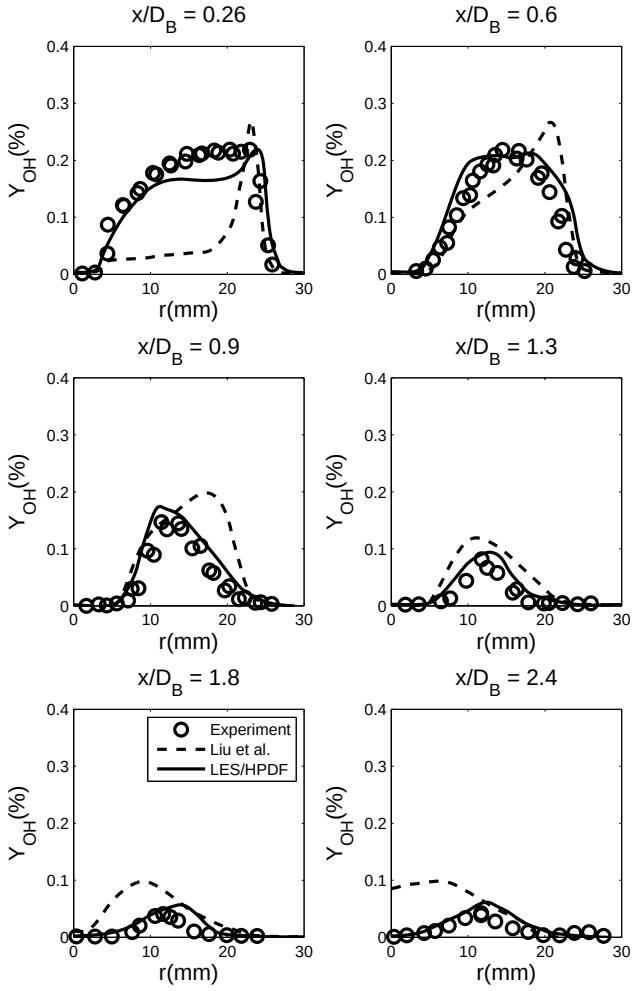

Figure 30: Radial plots of the Favre-averaged OH mass fraction at six axial locations, from $x = 0.26D_B$ to $x = 2.4D_B$, for the HM3 simulation.

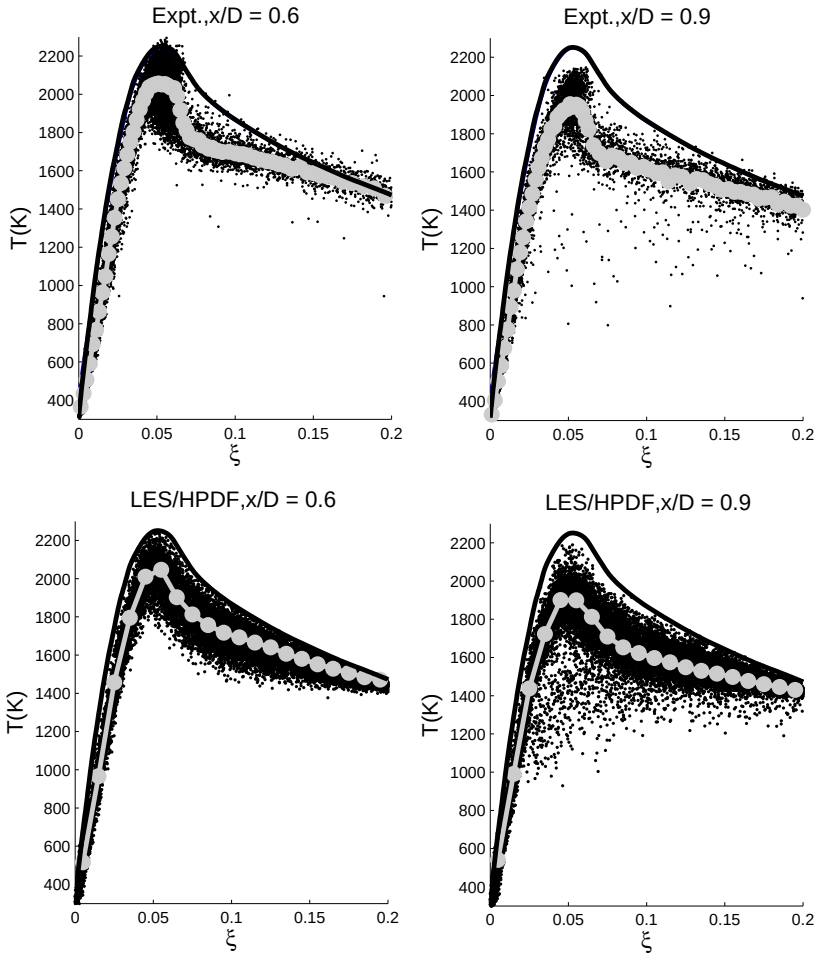

Figure 31: HM3 scatter plots of temperature plotted against mixture fraction, in the range $\xi \in [0, 0.2]$, for the axial locations $x = 0.6D_B$ and $x = 0.9D_B$. Conditional means are marked by the grey curve with circular symbols, and laminar flamelet temperatures are marked by the solid black curve. Top: experimental results. Bottom: LES/HPDF calculations.

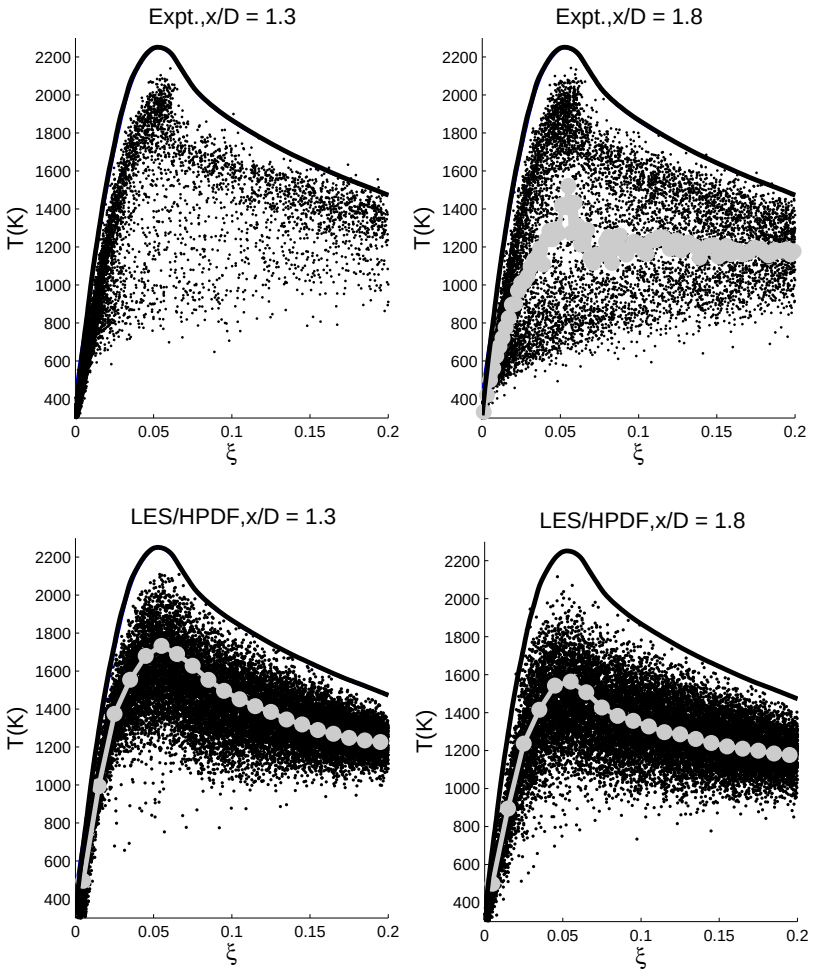

Figure 32: HM3 scatter plots of temperature plotted against mixture fraction, in the range $\xi \in [0, 0.2]$, for the axial locations $x = 1.3D_B$ and $x = 1.8D_B$. Conditional means are marked by the grey curve with circular symbols, and laminar flamelet temperatures are marked by the solid black curve. Top: experimental results. Bottom: LES/HPDF calculations.

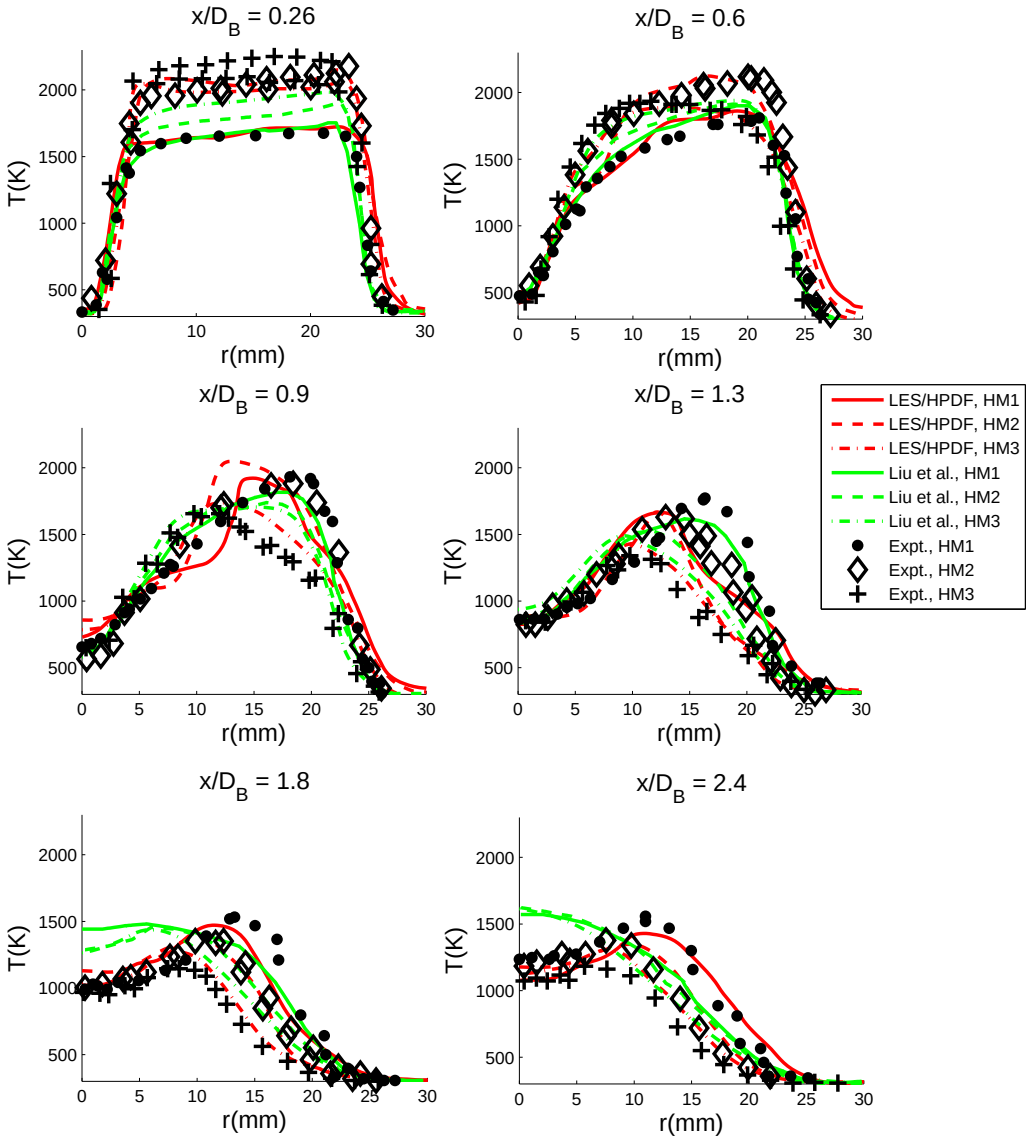

Figure 33: Comparison of the temperature profile variation from flame HM1 to HM2 to HM3. Symbols: experimental data. Red curves: LES/HPDF. Green curves: Liu et al.